Cell

Kiwa is a membrane-embedded defense supercomplex activated at phage attachment sites

Graphical abstract

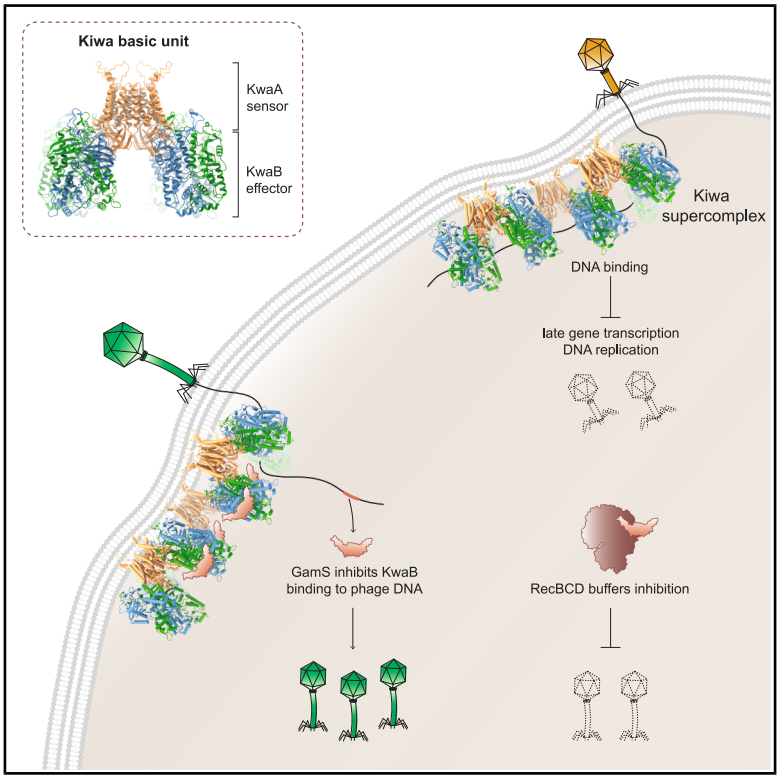

Authors

Zhiying Zhang, Thomas C. Todeschini, Yi Wu, ..., Eugene V. Koonin, Dinshaw J. Patel, Franklin L. Nobrega

Correspondence

pateld@mskcc.org (D.J.P.), f.nobrega@soton.ac.uk (F.L.N.)

In brief

Zhang, Todeschini, and Wu et al. show that the bacterial defense system Kiwa senses phage attachment at the membrane and assembles a transmembrane complex that halts infection by blocking phage DNA replication and late transcription. The activity of Kiwa is safeguarded against phage-encoded inhibitors by cooperation with the RecBCD system.

Highlights

- Kiwa is activated at membrane sites of phage attachment
- Kiwa forms a transmembrane supercomplex of KwaA and KwaB
- KwaB binds phage DNA to block replication and late transcription
- Phage-encoded DNA-mimic Gam inhibits Kiwa, but RecBCD preserves defense

Zhang et al., 2025, Cell *188*, 5862–5877
October 16, 2025
https://doi.org/10.1016/j.cell.2025.07.002

CellPress

CellPress
OPEN ACCESS

Cell

Article

Kiwa is a membrane-embedded defense supercomplex activated at phage attachment sites

Zhiying Zhang,[1,5,6,8] Thomas C. Todeschini,[2,8,9] Yi Wu,[2,8] Roman Kogay,[3] Ameena Naji,[2,10] Joaquin Cardenas Rodriguez,[2] Rupavidhya Mondi,[2,11] Daniel Kaganovich,[2] David W. Taylor,[4,5,6,7] Jack P.K. Bravo,[4,12] Marianna Teplova,[1] Triana Amen,[2] Eugene V. Koonin,[3] Dinshaw J. Patel,[1,*] and Franklin L. Nobrega[2,13,*]

[1]Structural Biology Program, Memorial Sloan Kettering Cancer Center, New York, NY, USA
[2]School of Biological Sciences, University of Southampton, Southampton SO17 1BJ, UK
[3]Computational Biology Branch, Division of Intramural Research, National Library of Medicine, National Institutes of Health, Bethesda, MD, USA
[4]Department of Molecular Biosciences, University of Texas at Austin, Austin, TX 78712, USA
[5]Interdisciplinary Life Sciences Graduate Programs, Austin, TX 78712, USA
[6]Center for Systems and Synthetic Biology, University of Texas at Austin, Austin, TX 78712, USA
[7]LIVESTRONG Cancer Institutes, Dell Medical School, Austin, TX 78712, USA
[8]These authors contributed equally
[9]Present address: RNA Therapeutics Institute, University of Massachusetts Chan Medical School, Worcester, MA, USA
[10]Present address: School of Molecular and Cellular Biology, University of Leeds, Leeds LS2 9JT, UK
[11]Present address: The William Harvey Research Institute, Barts and The London School of Medicine, Queen Mary University of London, Charterhouse Square, London EC1M 6BQ, UK
[12]Present address: Institute of Science and Technology Austria (ISTA), Klosterneuburg, Austria
[13]Lead contact
*Correspondence: pateld@mskcc.org (D.J.P.), f.nobrega@soton.ac.uk (F.L.N.)
https://doi.org/10.1016/j.cell.2025.07.002

SUMMARY

Bacteria and archaea deploy diverse antiviral defense systems, many of which remain mechanistically uncharacterized. Here, we characterize Kiwa, a widespread two-component system composed of the transmembrane sensor KwaA and the DNA-binding effector KwaB. Cryogenic electron microscopy (cryo-EM) analysis reveals that KwaA and KwaB assemble into a large, membrane-associated supercomplex. Upon phage binding, KwaA senses infection at the membrane, leading to KwaB binding of ejected phage DNA and inhibition of replication and late transcription, without inducing host cell death. Although KwaB can bind DNA independently, its antiviral activity requires association with KwaA, suggesting spatial or conformational regulation. We show that the phage-encoded DNA-mimic protein Gam directly binds and inhibits KwaB but that co-expression with the Gam-targeted RecBCD system restores protection by Kiwa. Our findings support a model in which Kiwa coordinates membrane-associated detection of phage infection with downstream DNA binding by its effector, forming a spatially coordinated antiviral mechanism.

INTRODUCTION

Bacteria and archaea have evolved a diverse repertoire of defense mechanisms against viral predation.[1–3] Widespread systems, such as CRISPR-Cas and restriction modification, not only revealed fundamental biological processes but also enabled transformative biotechnology applications, including gene editing, expression regulation, and RNA knockdown.[4]

However, the mechanisms of many recently discovered defense systems,[5–13] especially those associated with the membrane, remain poorly understood, as exemplified by the Kiwa system. Kiwa consists of two components: KwaA, a four-pass transmembrane protein, and KwaB, containing a DUF4868 domain of unknown function. The Kiwa system from *Escherichia coli* O55:H7 RM12579 protects against phages such as Lambda and SECphi18.[6] Kiwa is among the 20 most abundant defense systems across sequenced bacterial genomes,[1] suggesting a broad defense spectrum and evolutionary success. Yet, how Kiwa senses phages and provides protection remains elusive. Here, we apply structure-function approaches to uncover the molecular basis of Kiwa defense, showing that Kiwa forms a transmembrane supercomplex with a basic repeating unit consisting of a KwaA tetramer bound to KwaB dimers. Kiwa is activated at the site of phage attachment, where KwaB binds phage DNA via its DUF4868 domain, disrupting phage replication and late transcription without inducing cell death. KwaB alone can bind phage DNA but is insufficient for defense, requiring spatial and conformational coordination with KwaA. We demonstrate that Kiwa and RecBCD cooperate to resist phage-encoded inhibitors such as the DNA-mimic Gam. Although Gam targets

both systems, it cannot inhibit them simultaneously when they co-occur, illustrating how immune system interplay enhances bacterial resilience.

RESULTS

Kiwa provides broad protection against phages and plasmids

To investigate the diversity and abundance of Kiwa, we searched 223,143 prokaryotic genomes from the Prokaryotic Antiviral Defence LOCator (PADLOC) database.[13,14] Kiwa was identified in 9,582 genomes, including 1,713 *E. coli* genomes. We dereplicated KwaA and KwaB protein sets at 90% sequence identity and reconstructed their phylogenies. Although deep branches were unresolved, both KwaA and KwaB grouped into three distinct clusters (Figure 1A), with the *E. coli* O55:H7 RM12579 Kiwa included in cluster 1 (purple). Kiwa is particularly prevalent in bacterial orders *Bacillales* and *Enterobacterales* (Figure 1B). The phylogeny of Kiwa deviates from the host species taxonomy, indicating extensive horizontal gene transfer (Figure 1A). Partial incongruence between KwaA and KwaB trees suggests occasional independent transfer of the two genes (Figure 1B).

To identify mobile genetic elements (MGEs) associated with Kiwa operons, we analyzed genomic neighborhoods. More than half of dereplicated *kwaA* (673/1,257; 53.5%) and *kwaB* (676/1,261; 53.6%) genes co-localized with MGEs, including 197/198 prophages, 105/110 plasmids, and 304/302 genomic islands for KwaA and KwaB, respectively (Figure 1A). In 70 Kiwa loci (19 in the dereplicated dataset), *kwaB* is split into two genes. The tree topology suggests multiple, independent *kwaB* gene fissions (Figure 1A).

As defense system variants often differ in phage specificity,[5,17,18] we cloned five Kiwa systems from different clusters into *E. coli* BL21-AI, which lacks endogenous Kiwa (Figures 1C and S1A). When challenged with a panel of eight phages, all systems provided defense, each with unique specificity and efficacy (Figures 1D and S1B). Kiwa also reduced plasmid conjugation over twofold, with the exception of Kiwa from *Ralstonia mannitolilytica* SN82F48 (Figure 1E).

These results show that Kiwa provides broad defense against both phage infection and plasmid conjugation, with system-specific variations in activity.

KwaA forms a structurally variable homotetramer

To investigate Kiwa function, we characterized the structure of the transmembrane protein KwaA. Gel filtration indicated that KwaA forms oligomers (Figure S2A). Cryogenic electron microscopy (cryo-EM) in lauryl maltose neopentyl glycol (LMNG) detergent revealed two structural states with resolutions of 3.69 and 4.28 Å (Figures S2B and S2C; Table S1). The higher-resolution map allowed confident model building, with well-defined side chains (Figure S2D). In both states, KwaA forms a homotetramer with an hourglass-like shape (Figures 2A and 2B).

Each KwaA protomer contains four transmembrane helices (TM1–4), two periplasmic loops (PL1 and 2), one intracellular loop (ICL1), and the intracellular C terminus. ICL1 and the C terminus form a six-stranded β-barrel (Figure 2C). The 3.69-Å map exhibits C2 symmetry (Figure 2A), whereas the 4.28-Å map shows C4 symmetry (Figure 2B). In the C2-symmetric structure, two of the four KwaA protomers take a different shape than the other two (Figure S2E), especially in PL2 and TM4, altering helix-helix interactions. As a consequence, the central arrangement of transmembrane helices differs between the structures: the C2 state (Figure 2A) shows an asymmetric TM3-TM4 interface (Figure 2D), whereas the C4 state (Figure 2B) features a symmetric interface formed by TM3 from all protomers (Figure 2E).

Both states share interface I, involving TM1 and TM3 of one protomer and TM3 and TM4 of an adjacent protomer, stabilized by hydrophobic and π-π interactions (Figures 2F and S2F). The C2 structure also features interface II (Figure 2D), where TM4 interacts extensively with TM1 and TM3 of another protomer (Figure S2F). PL2 is also reorganized in the C2 state, linking two diagonal protomers. In the C2-symmetric structure, we observed an LMNG detergent molecule inserted into the central transmembrane cavity (Figures 2A and S2G). The hydrophilic heads of LMNG extend outward, whereas the two hydrophobic tails interact with KwaA residues inside the membrane-spanning region (Figure S2G).

Thus, the transmembrane subunit KwaA forms a homotetramer that adopts two distinct conformations.

KwaB forms a stable dimer

We next determined the structure of KwaB. The 3.9-Å crystal structure revealed a dimer-of-dimers topology in the crystal lattice, with interactions between the C-terminal region of one monomer from one dimer and the α2 helix from a separate dimer (Figure S3A; Table S1).

To evaluate whether this dimer-of-dimers arrangement reflected the physiological state, we performed mass photometry under crystallization buffer conditions, finding that ∼95% of the particles matched the expected size of a tagged KwaB dimer (∼79 kDa), with only a minor fraction representing larger oligomers (Figure S3B). Thus, KwaB predominantly exists as a dimer in solution.

To explore the dimer-of-dimers interface, we modeled KwaB tetramer using AlphaFold 3 (AF3). The C-terminal dimer interface showed high confidence (predicted Local Distance Difference Test [pLDDT] > 90), whereas the N-terminal loop (N134-L174) involved in the crystallographic contacts had low confidence (pLDDT < 50) (Figure S3C), suggesting that the crystallographic dimer-of-dimers configuration is an artifact of crystal packing.

Supporting this, we solved the crystal structure of the KwaB dimer at 3.6-Å resolution (Table S1) and obtained a 3.86-Å cryo-EM density map of KwaB within the KwaAB complex (see details below; Table S1). Local refinement resolved key stabilizing features of the KwaB dimer: the N-terminal flexible loop (N134-L174) and the β-turn motif in the C-terminal domain (S292-E315) (Figure S3D).

KwaB comprises two domains: an N-terminal region (residues 1–185) with a central parallel β-sheet and a βαβ hairpin (showing no structural similarity to known proteins), and a C-terminal DUF4868-containing region (residues 186–315) (Figure 2G). Both domains contribute to KwaB dimer formation (Figure 2G). In some lineages, *kwaB* is split into two genes (Figure S1A).

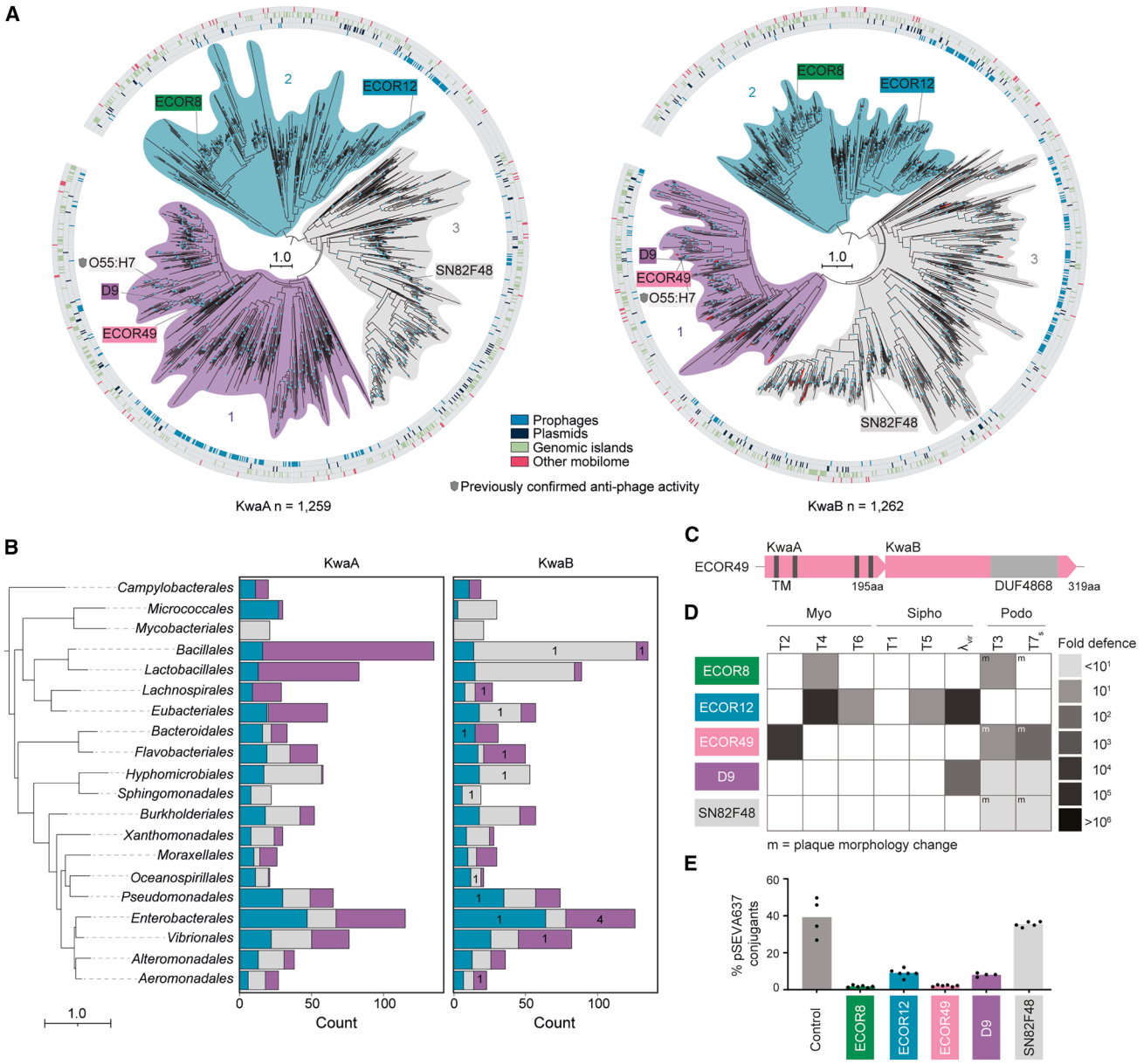

Figure 1. Diversity of Kiwa systems and patterns of defense against phage infection and plasmid conjugation

(A) Phylogenetic trees of KwaA and KwaB from the dereplicated dataset. Kiwa operons tested in this study are annotated, and previously validated anti-phage Kiwa operons are indicated with a shield. Split KwaB genes are annotated in red. Scale bar shows substitutions per site, and nodes with ≥80% bootstrap support are in cyan. Co-localization with MGEs is shown in the outer circles. "Other mobilome" denotes proximity to ≥2 hallmark mobilome genes,[15] not classified as plasmid, prophage, or genomic island.

(B) Distribution of KwaA and KwaB across 20 bacterial orders containing the most dereplicated Kiwa components. The Genome Taxonomy Database (GTDB)-based[16] species tree is scaled in substitutions per site. Bar colors match the clusters in (A), and numbers in the KwaB bar plot indicate instances of *kwaB* split into two genes.

(C) Representative Kiwa operon from *Escherichia coli* reference collection ECOR49. TM, transmembrane domain. DUF, domain of unknown function.

(D) Anti-phage activity of five Kiwa operons shown as fold-protection in plating assays versus YFP-expressing controls. Operons are from *E. coli* ECOR8, ECOR12, ECOR49, D9, and *Ralstonia mannitolilytica* SN82F48. m, plaque morphology change.

(E) Anti-conjugation activity of five Kiwa operons shown as percentage of conjugants (pSEVA637 transfer from S17-1 donors) relative to total cells. Bars represent mean of ≥4 replicates with individual data points.

See also Figure S1.

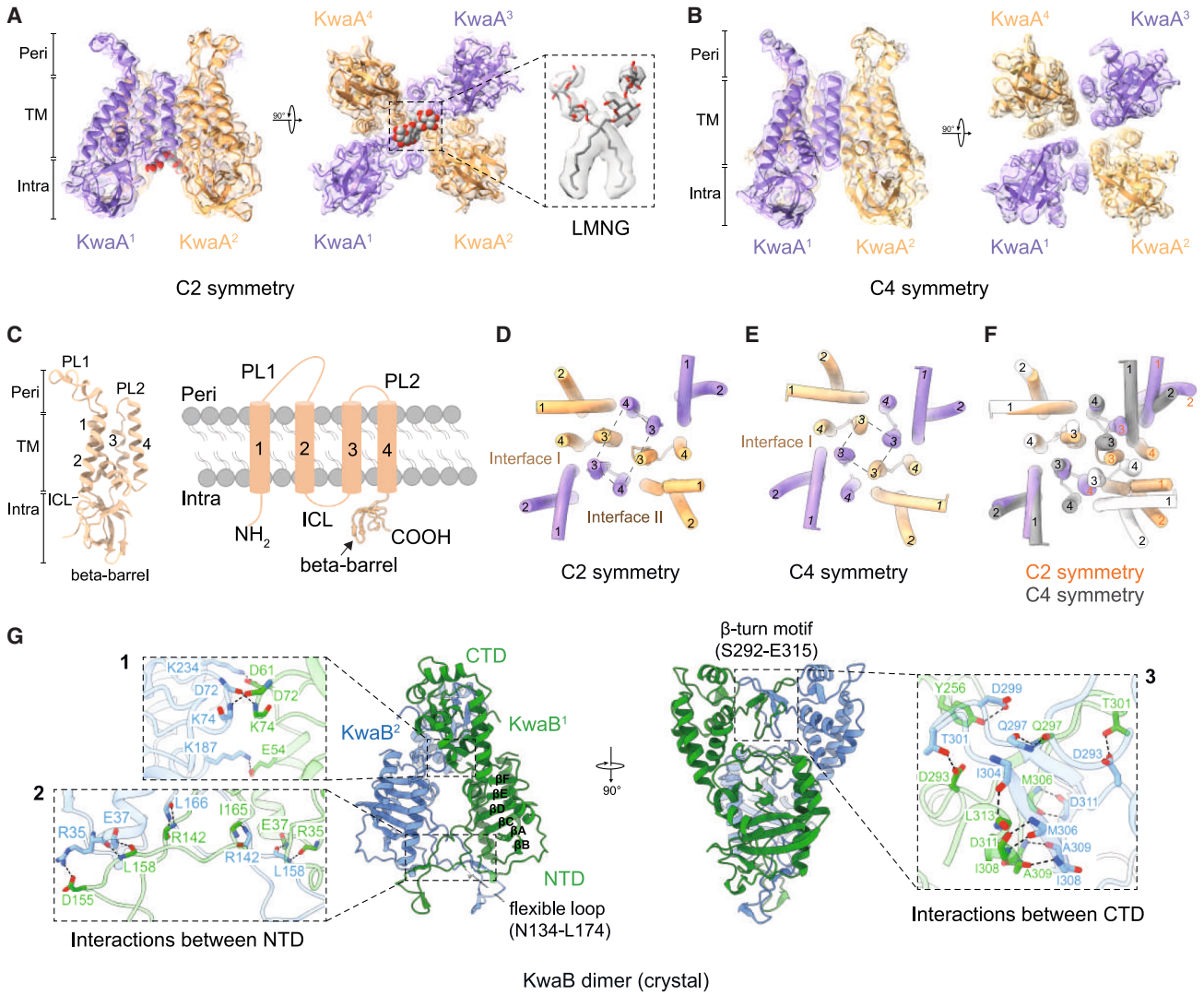

Figure 2. Structures of KwaA and KwaB

(A and B) Cryo-EM structure of KwaA tetramer with (A) C2-symmetry and (B) C4-symmetry (monomers in purple and orange), and an LMNG molecule (boxed) is visible in the central channel. Periplasmic (peri), intracellular (intra), and transmembrane (TM) regions indicated.

(C) Cryo-EM and schematic views of transmembrane (TM1–4), periplasmic loops (PL1 and PL2), intracellular loop (ICL), and intracellular beta-barrel of a KwaA monomer.

(D and E) Helical segments lining the central channel in KwaA tetramer with (D) C2-symmetry and (E) C4-symmetry, with interfaces labeled.

(F) Structural superposition of helical segments of KwaA tetramers with C2- and C4-symmetry.

(G) Cryo-EM structure of the KwaB dimer (green and blue), highlighting the flexible loop (N134-L174) in the N-terminal domain (NTD) and β-turn motif (S292-E315) in the C-terminal domain (CTD). Insets show: (1) NTD-NTD interactions, stabilized by salt bridges (E54-K187 and D61-K234) and main-chain interactions, (2) additional NTD interactions primarily via the flexible loop and a salt bridge (R35-D155), and (3) β-turn motif in CTD, stabilized by hydrogen bonds (Y256-D299 and T301-D293) and main-chain interactions.

See also Figures S2 and S3.

AlphaFold2 (AF2) predictions of these split proteins showed that each closely resembles the respective domain of KwaB (Figures S3E–S3G). Multimeric structure predictions further indicated that tetramers formed by split KwaB resemble the dimeric architecture of the single-chain version (Figure S3H–S3J). The split KwaB proteins likely evolved via multiple, independent fissions of the ancestral single protein while retaining their domain folds and functional equivalence.

KwaA and KwaB form a fence-like TM supercomplex

To investigate the roles of KwaA and KwaB in Kiwa defense, we tested single-gene deletions. Loss of either gene abolished defense, indicating both are essential. Truncating the TM domains in KwaA also disrupted defense, highlighting the importance of membrane localization (Figure 3A).

Co-expression and gel filtration revealed low- and high-molecular-weight species, indicating that KwaA and KwaB form a

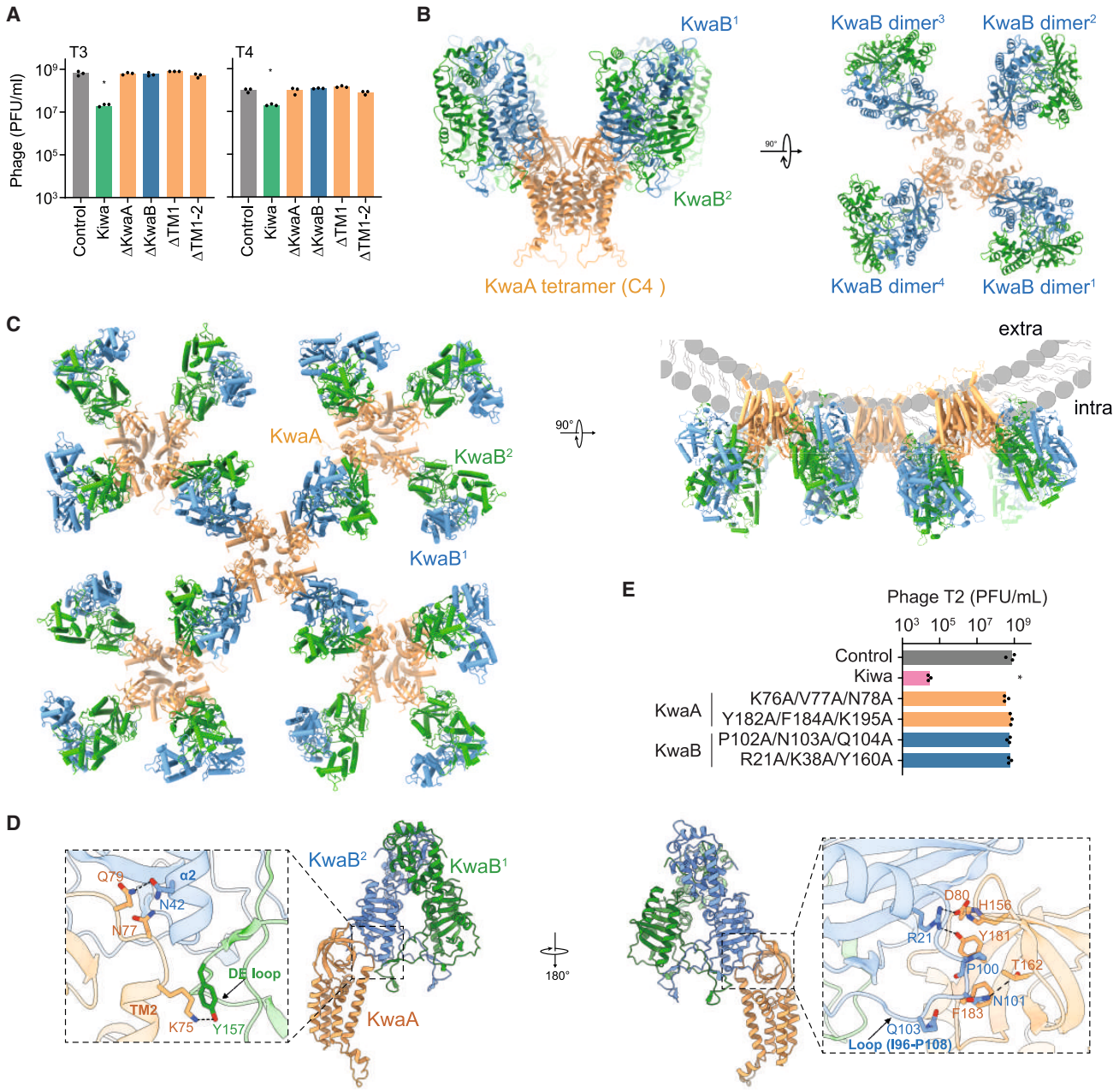

Figure 3. KwaA and KwaB form a supercomplex

(A) Defense of Kiwa mutants against T3 and T4. Plaque-forming unit (PFU)/mL shown for each strain. *$p < 0.05$ compared with Kiwa (two-way ANOVA). Bars show mean ($n = 3$) with individual data points.

(B) Cryo-EM structure of the higher molecular weight KwaAB complex: four KwaB dimers (blue and green) bound to a KwaA tetramer (orange).

(C) Model of a fence-like KwaAB supercomplex on a curved cell membrane.

(D) Interactions between a KwaA monomer and KwaB dimers in the KwaAB complex. Insets show smaller (left) and larger (right) interfaces.

(E) Impact of point mutations on KwaA and KwaB ECOR49 defense against T2. PFU/mL shown for each strain. *$p < 0.05$ (two-way ANOVA). Bars represent mean ($n = 3$) with individual data points.

See also Figure S4.

complex (Figure S4A). Cryo-EM of the high-molecular-weight species showed a fence-like supercomplex (Figure S4B). Symmetry analysis and classification resolved the minimal unit at a 3.7-Å resolution: a KwaA tetramer bound to four KwaB dimers (Figures 3B and S4B–S4E; Table S1). The KwaB dimer in the KwaAB complex closely resembles its crystal structure (root-mean-square deviation [RMSD] = 0.588 Å, Figure S4F), and KwaA monomers adopted conformations similar to the C4

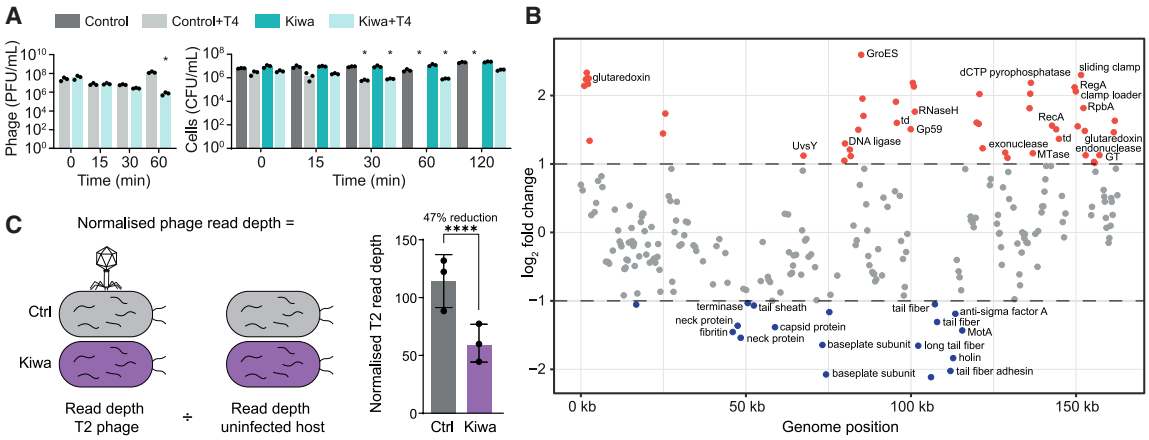

Figure 4. Kiwa reduces late phage gene transcription and genome replication

(A) Phage (PFU/mL) and cell (colony-forming unit [CFU]/mL) titers post-infection (MOI = 10) in control and Kiwa-expressing cells. Means (n = 3) shown with individual data points. *p < 0.05 from controls (two-way ANOVA).

(B) Transcriptomic changes in Kiwa-expressing versus control cells at 15 min post T2 infection. Genes upregulated in Kiwa cells are in red, and those downregulated are in blue.

(C) Quantification of T2 DNA in infected Kiwa-expressing and control cells. Phage read depth was normalized to host genomic DNA in uninfected cells (schematic, left). Bars show mean ± SD (n = 3). ****p < 0.0001 (two-tailed unpaired t test).

structure (Figures 3B and S4B), with local rearrangements at KwaB interaction sites (RMSD = 1.24 Å; Figure S4G). No KwaB dimer-of-dimers configuration was observed, compatible with a crystallization artifact. Instead, each KwaB dimer bridges two KwaA tetramers (Figures 3C and S4H). Each KwaA monomer engages both KwaB protomers through two main interfaces.

In the smaller interface, the flexible DE loop (N134-L174, between β-sheets D and E) of KwaB contacts TM2 of KwaA, where Y157 of the loop forms a hydrogen bond with K75 of TM2 (Figure 3D, left). At the lateral surface of the C-terminal β-barrel, α2 helix of KwaB lies adjacent to ICL1 of KwaA. Here, Q79 of KwaA potentially forms a hydrogen bond with N42 of KwaB, whereas N77 interacts with the main chain of α2, further stabilizing the interface. Triple mutations in KwaA residues involved in this interaction (K75/V76/N77 and K76A/V77A/N78A in ECOR49 [71.6% similarity to KwaA from O55:H7]) abolished defense (Figures 3E and S4I).

In the larger interface (Figure 3D, right), a KwaB loop near β-sheet C (I96-P108) lies over the KwaA β-barrel channel. P100 from KwaB is deeply embedded, surrounded by KwaA residues H156, Y181, and F183, forming π-π interactions. H156 engages in a cation-π interaction with R21 from beta-sheet A of KwaB, the latter likely forming a hydrogen bond with Y181 and a salt bridge with D80 of KwaA. Additional polar contacts involve N101 and Q103 from KwaB and T162 and the main chain of KwaA, respectively. Mutations in critical KwaA (C-terminal beta-barrel; Y181/F183/K194 and Y182A/F184A/K195A in ECOR49) and KwaB (R21/R35/Y157 and R21A/K38A/Y160A in ECOR49; P100/N101/Q103 and P102A/N103A/Q104A in ECOR49) residues at this interface abolished defense (Figure 3E).

KwaB dimers serve as anchors for supercomplex assembly (Figure 3C). Alignment of basic units through KwaB dimers revealed that the KwaAB supercomplex adopts a bent transmembrane conformation, opposite to the natural membrane curvature (Figure 3C). The C4 symmetry of KwaA favors this assembly, whereas C2 symmetry models predicted increased curvature (Figure S4J), suggesting that KwaA conformation influences membrane interaction.

An additional band coeluting with the high-molecular-weight KwaAB complex (Figure S4A, right) corresponded to the heptameric, closed-state mechanosensitive channel MscK[19] (Figures S4B and S4K). However, MscK was not required for defense, as Kiwa remained active in MscK-deficient cells (Figure S4L).

Thus, Kiwa forms a transmembrane supercomplex composed of a KwaA tetramer bound to four KwaB dimers as its basic repeating unit, where KwaB homodimers serve as structural anchors for supercomplex assembly.

Kiwa protects cells by disrupting phage replication and late transcription

To investigate how Kiwa confers protection, we investigated whether it induces abortive infection or mutual destruction, scenarios in which infected cells die, preventing phage propagation.[20,21] At high phage pressure (MOI = 10), Kiwa-expressing cells remained largely viable while phage titers dropped substantially (Figure 4A). By contrast, control cells lacking Kiwa were cleared below detection limits. Thus, Kiwa prevents productive infection without killing the host.

To determine the affected stage of the phage cycle, we performed RNA sequencing (RNA-seq) 15 min post T2 infection. Of the 255 phage genes, expression of 187 was unchanged in Kiwa-expressing cells, whereas 18 late genes, encoding structural components and terminase, were substantially downregulated ($\log_2$-fold change < −1) (Figure 4B; Table S2). Conversely, 59 phage genes were upregulated, including those involved in DNA replication (e.g., helicase loader), DNA repair and recombination (e.g., UvsY and RecA), DNA modification (Dam), and late

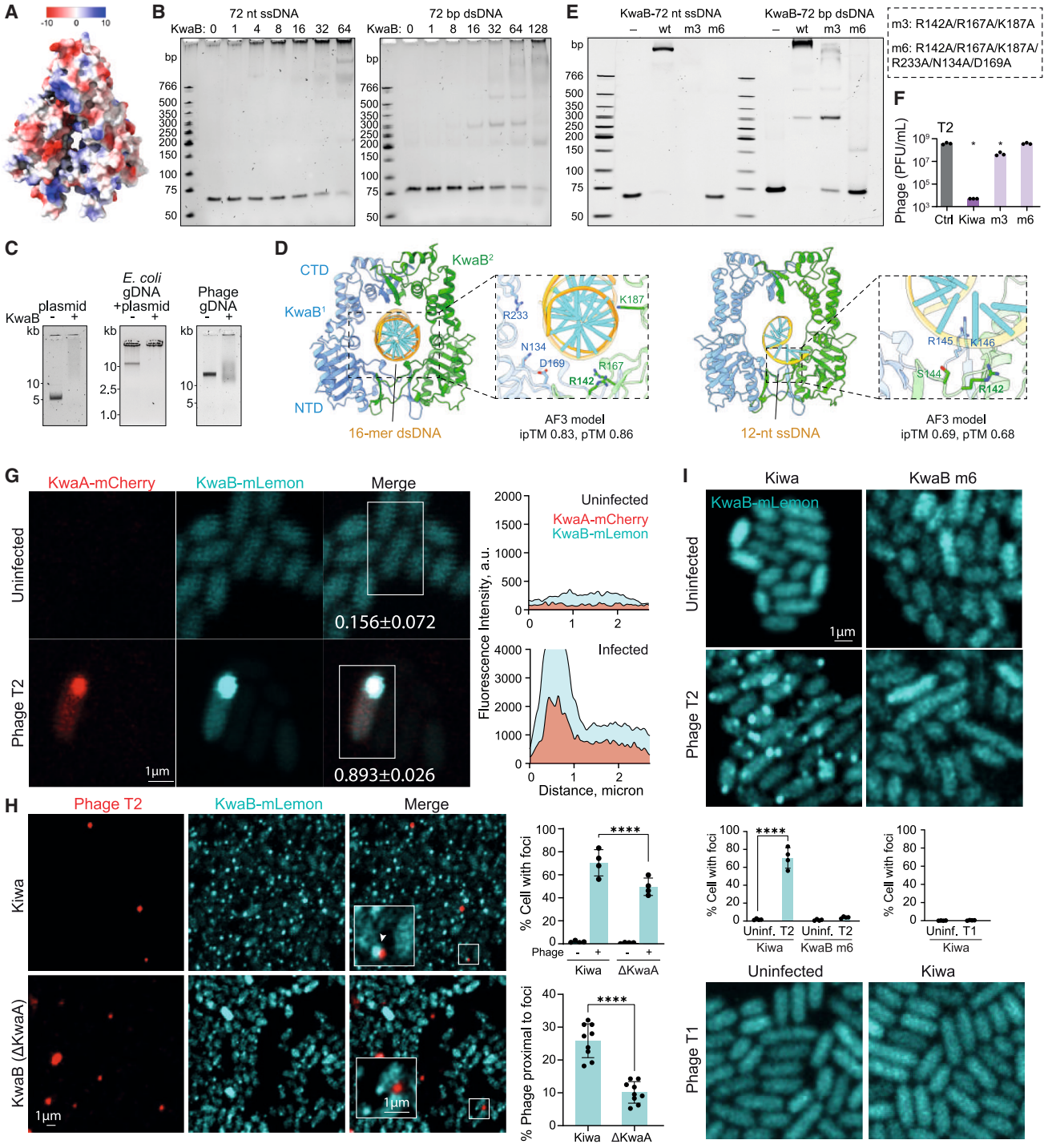

Figure 5. KwaB binds phage DNA and forms infection-site-specific foci in a KwaA-dependent manner

(A) Electrostatic surface representation of KwaB dimer.

(B) EMSA with increasing concentrations of KwaB dimer and 72 nt ssDNA (left) or dsDNA (right) (10 nM) (KwaB-to-DNA ratios on top of the gel).

(C) EMSA with KwaB (350 nM) and circular plasmid DNA, bacterial or phage genomic DNA (50 ng).

(D) AlphaFold3 (AF3) models of KwaB bound to 16-mer dsDNA (left) or 12-nt ssDNA (right), showing DNA positioned between the dimer interface. Insets highlight predicted protein-DNA contacts.

(E) EMSA with wild-type and mutant KwaB (2.56 µM dimer) and ssDNA (left) or dsDNA (right) (10 nM), testing impact of DNA-binding residue mutations (m3 and m6).

(F) Impact of m3 and m6 mutations on Kiwa defense against T2. Phage titers represent means (n = 3); *p < 0.05 (two-way ANOVA).

(legend continued on next page)

transcription activation (e.g., GP45.1 and RpbA). Because late transcription in T4-like phages depends on ongoing DNA replication,[22] we hypothesized that Kiwa impairs replication. To test this, we quantified phage DNA in infected cells by comparing phage and host read depth, correcting for phage-induced host DNA degradation. Phage DNA levels were reduced by ~47% in Kiwa-expressing cells (Figure 4C), consistent with stalled replication. This reduction correlated with transcriptional upregulation of phage repair and recombination genes that are essential for reassembling functional replication forks.[23–26]

Thus, Kiwa arrests phage reproduction by impairing DNA replication, resulting in a failure to express late-stage structural and packaging genes.

KwaB binds phage DNA and forms infection-site-specific foci in a KwaA-dependent manner

To elucidate the Kiwa defense mechanism, we investigated the role of KwaB, the cytoplasmic component of the complex. The sequence-based alignment-free protein function predictor (SPROF-GO)[27] predicted nucleic acid binding, and electrostatic surface analysis revealed a positively charged central channel in the KwaB dimer, suggesting a DNA-binding site (Figure 5A). Electrophoretic mobility shift assays (EMSAs) confirmed that KwaB binds both linear single-stranded DNA (ssDNA) and double-stranded DNA (dsDNA) (Figure 5B), as well as plasmid and phage DNA (Figure 5C). Although smearing was initially observed with phage DNA, nuclease assays detected no cleavage (Figure S5A), indicating non-degradative binding. The smearing likely reflects heterogeneous binding, conformational effects on the DNA, or partial dissociation during electrophoresis.[28]

AF3 models of a KwaB dimer bound to dsDNA/ssDNA showed high confidence, with DNA threading through the positively charged central channel and stabilized by residues in the DUF4868 domain (Figures 5D and S5B). The two DNA-bound models were similar (RMSD: 0.711 Å; Figure S5C) but distinct from the DNA-free (apo) form (Figures 2G, 5D, and S5D; RMSD = 12.653 Å), with DNA binding inducing a major conformational rearrangement from a "V"- to "U"-shaped dimer (Figure S5D). Mutating all predicted dsDNA-contacting residues (m6: R142A/R167A/K187A/R233A/N134A/D169A) abolished defense and severely reduced DNA binding (Figures 5E, 5F, S5E, and S5F).

AF3 models of DNA-bound KwaAB showed moderate confidence (dsDNA: interface predicted TM-score [ipTM] 0.46 and predicted TM-score [pTM] 0.49; ssDNA: ipTM 0.64 and pTM 0.7) and preserved KwaA-KwaB interfaces (dsDNA: RMSD 0.919, ssDNA: RMSD 0.729 Å; Figure S5G). However, DNA-bound KwaB dimers were displaced ~15.9 Å from their apo position, creating steric clashes with adjacent KwaA subunits in the static cryo-EM model (Figure S5H), suggesting that DNA binding triggers supercomplex rearrangement.

In vivo, fluorescently tagged KwaA and KwaB formed co-localized foci at cell poles upon T2 infection (Figures 5G and S5I), suggesting that the complex is stable during infection and accommodates phage DNA through structural flexibility. Because phage DNA is typically ejected at the poles,[29] we asked whether KwaB localizes to the site of phage entry and whether such localization depended on KwaA.

Using SYTOX Orange-stained T2, we found that KwaB foci often formed near attached phage particles before DNA ejection, as indicated by the SYTOX signal remaining within the phage capsid (Figure 5H). Foci appeared in 70% ± 11% of infected cells expressing KwaA, versus 50% ± 8% for cells without KwaA. Furthermore, 27% ± 5% of KwaB foci co-localized with adsorbed phages in the presence of KwaA, compared with only 10% ± 3% without KwaA (Figure 5H). Thus, the foci-forming capability and infection-site specificity of KwaB substantially depend on KwaA. KwaB alone does not confer defense (Figure 3A), supporting a model in which KwaB is activated through KwaAB complex formation.

DNA binding was also required for KwaB foci formation, as the m6 mutant failed to form foci in T2-infected cells, and infection with T1 (a non-targeted phage) also failed to induce foci (Figure 5I). Given the affinity of KwaB for both dsDNA and ssDNA (Figure S5J) and its localization to DNA ejection sites, we propose that KwaB binds ejected phage DNA, likely via ssDNA junctions at replication forks. This binding is essential for defense, and the observed drop in phage DNA levels and late gene transcripts in Kiwa-expressing cells (Figure 4) suggests that KwaB binding impedes replication fork progression.

Thus, KwaB binds incoming phage DNA at the infection site via the DUF4868 domain, forming foci in a KwaA-dependent manner. This interaction disrupts phage DNA replication and late transcription, blocking phage propagation.

Kiwa is activated at the membrane and may sense phage infection via periplasmic loops of KwaA

To investigate Kiwa activation, we isolated T3 and T7Select (T7s) phage mutants that escape Kiwa defense (Figure 6A). Sequencing revealed mutations in genes encoding inhibitors of the stationary phase σ^S subunit (RpoS) of host RNA polymerase (RNAP) (T7s gp5.7, T3 T3p30)[30,31] and tail fiber genes (T7s gp17, T3 T3p48) (Figure 6A; Table S3). Expressing the RpoS inhibitors in *trans* restored Kiwa protection, whereas expressing tail fibers did not (Figure 6B).

We showed that KwaAB foci form at phage attachment sites before DNA ejection (Figures 5G–5I), indicating membrane-localized activation. Because phage-encoded proteins like gp5.7 and T3p30 are expressed post-ejection, they likely act at

(G) Confocal microscopy showing co-localization of mCherry-KwaA (red) and mLemon-KwaB (blue) in T2-infected cells. Right: line plots show fluorescence intensity along the indicated axis.

(H) Confocal imaging of KwaB-mLemon foci in T2-infected cells with or without KwaA. Top right: percentage of cells with visible foci. Bottom right: percentage of foci co-localizing with SYTOX-stained T2 particles. Data show mean ± SD from ≥4 replicates ($n \geq 400$ cells); ****$p < 0.0001$ (unpaired t test).

(I) Top: KwaB m6 mutant fails to form foci in T2-infected cells. Bottom: KwaB-mLemon does not form foci in T1-infected cells. Middle: quantification of cells displaying foci across conditions. Data show mean ± SD from four biological replicates ($n \geq 500$ cells). ****$p < 0.0001$ (unpaired t test).

See also Figure S5.

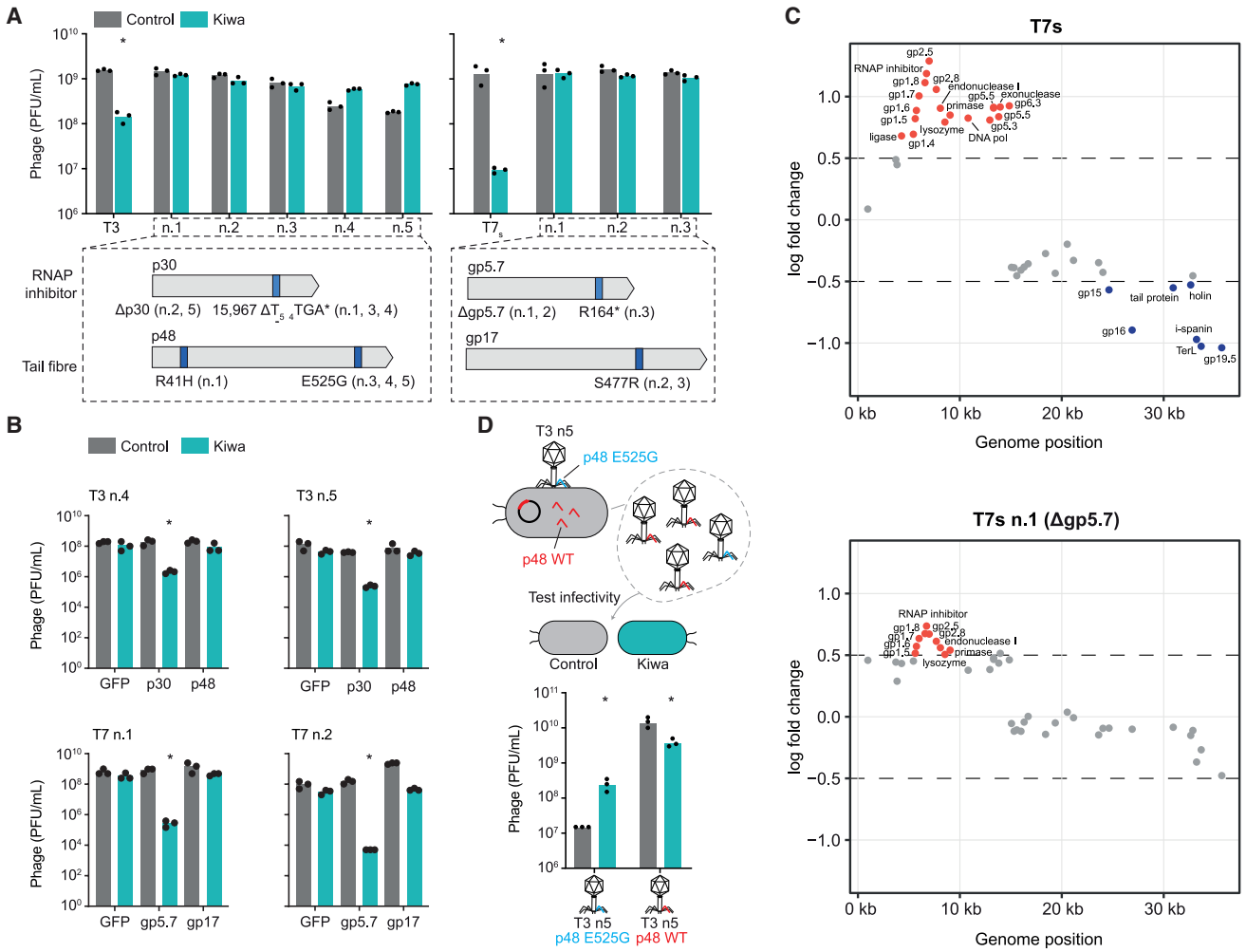

Figure 6. Kiwa escaper mutants implicate the phage tail fiber in defense activation and the RNAP inhibitor in effector inactivation

(A) Phage titers (PFU/mL) of wild-type (T3 and T7s) and mutant phages (*n*) in control (YFP) and Kiwa-expressing cells. Bars show means ($n = 3$) with individual data points; $^*p < 0.05$ (two-way ANOVA). Mutations in escapers are indicated below the graphics, and the full list is in Table S3.

(B) Complementation with T3p30 or T7s gp5.7 restored Kiwa defense against escape phages, while T3p48 and T7s gp17 did not. Bars show means ($n = 3$) with individual data points; $^*p < 0.05$ (two-way ANOVA).

(C) RNA-seq of T7s (top) and T7s n.1 (Δgp5.7, bottom) infection in Kiwa or control cells. Log_2-fold changes in phage gene transcription across the genome are shown. Early genes are in red, late genes are in blue.

(D) Top: diagram of T3 n5 escaper mutant (tail fiber E525G, blue) complemented by propagation in cells expressing wild-type T3p48 (red). Bottom: phage titers of the escaper and complemented version in control and Kiwa-expressing cells. Bars show mean ($n = 3$) with individual data points. $^*p < 0.05$ (two-way ANOVA). See also Figure S6.

or engage with the effector stage of the response. To test this, we performed RNA-seq on Kiwa-expressing cells infected with either wild-type T7s or a gp5.7 mutant (T7s n1). For wild-type T7s, early phage genes were upregulated and late genes suppressed, consistent with the findings for T2 (Figures 4B and 6C). In the gp5.7 mutant, early genes were upregulated, but late gene expression was unaffected, suggesting that Kiwa was activated, but KwaB effector activity was impaired. Given that wild-type gp5.7 inhibits the RNAP RpoS without strongly affecting T7 replication,[30] its loss in phage escapers may alter RNAP activity or composition, affecting KwaB interference with transcription. One possibility is that the altered RNAP function in the escape mutants reduces the susceptibility of phage late gene transcription to KwaB-mediated interference, as suggested by the lack of late gene suppression in RNA-seq. This would be consistent with KwaB acting by disrupting transcription complexes, depending on the configuration of the host RNAP machinery.

These results, together with the dependency of KwaB function on KwaA, support a model where KwaA acts as the membrane sensor that activates the DNA-binding effector KwaB. To test whether tail fibers contribute to activation, we propagated T3 escapers with mutated tail fiber (T3p48) in cells expressing wild-type T3p48 in *trans*. Two mutants (T3 n4 and n5)

were selected for their high escape efficiency (Figure 6B). Incorporation of the wild-type tail fiber was confirmed in T3 n5 particles by restored infectivity in the lipopolysaccharide (LPS) mutant strain ΔwaaJ, which T3 n5 cannot infect efficiently unless complemented with the wild-type fiber (Figure S6A). When these complemented phages infected Kiwa-expressing cells, defense was partially restored, implicating the tail fiber in Kiwa activation (Figure 6D).

To explore the potential Kiwa sensor, we examined the periplasmic loops of KwaA. PL1 (25 amino acids [aa]) and PL2 (7 aa) are both surface-exposed, but PL1 is more flexible, as indicated by weak electron density in the C4 KwaA tetramer structure (Figure S6B). Both loops are among the least conserved regions in KwaA, and neither contains identifiable conserved motifs (Figure S6C). These properties—exposure, flexibility, and variability—are commonly associated with pathogen sensors across diverse prokaryotic and eukaryotic immune systems.[32–37]

KwaA shares a four TM topology, with short and long periplasmic loops, with eukaryotic tetraspanins,[38] whose long extracellular loops (LELs) sense viral ligands and trigger protein clustering.[39] Although PL1 of KwaA is located in the periplasm and is unlikely to contact the tail fiber directly, phage attachment could trigger structural changes that propagate to the inner membrane and are sensed by PL1. This signal could induce local conformational changes in KwaA that would be transmitted to the intracellular side to activate or cluster KwaB, which binds to the cytoplasmic face of TM2. As observed for tetraspanins that induce the formation of higher-order protein complexes upon sensing a viral cue,[40] KwaAB foci only form upon phage infection (Figures 5G–5I). Although KwaB binds DNA, it does not protect without KwaA, confirming that the full complex is essential for defense activation.

Thus, Kiwa is triggered at the membrane, likely via periplasmic sensing of phage-induced structural perturbations. The variable, flexible PL1 loop of KwaA is consistent with a sensor function. Phages escape Kiwa either by impairing effector function (via RpoS inhibitors) or by reducing activation efficiency (via tail fiber mutations), highlighting two complementary evasion strategies.

Kiwa is antagonized by phage DNA-mimic protein Gam

Phages often encode proteins that counteract bacterial immunity,[41,42] including DNA mimics that prevent DNA-targeting defenses from accessing phage genomes.[43–45] Because KwaB binds DNA, we hypothesized that DNA mimics inhibit Kiwa.

We tested the effects of two well-characterized DNA-mimic proteins, T7 Ocr[45] and Lambda Gam,[46] on Kiwa defense against T4, which lacks both inhibitors. Gam, but not Ocr, strongly inhibited Kiwa, reducing protection by ~100-fold (Figure 7A). Similarly, a Lambda mutant lacking active Gam[47] was ~100-fold more sensitive to Kiwa than wild-type Lambda (Figure S7A).

To explore the Gam-KwaB interaction, we performed bacterial adenylate cyclase-based two-hybrid and co-purification assays, both supporting direct interaction (Figures S7B and S7C). Although structural resolution of the complex was hindered by aggregation and precipitation, AF2 modeling predicted that Gam binds in the central positively charged channel of the KwaB dimer, mimicking DNA (Figures 5D and 7B). A pair of Gam dimers inserted into this channel in the model (Figure 7B), triggering a conformational shift from a V- to U-shape, similar to DNA binding (RMSD = 12.215 versus 12.653 Å; Figures S5D and S7D).

The structures of KwaB-Gam and KwaB-DNA complexes were nearly identical (RMSD = 1.158 Å; Figure S7E), suggesting that Gam functions as a dominant negative inhibitor of DNA binding by KwaB. Although the model had moderate confidence (iPTM 0.483, pTM 0.555), the KwaB-Gam interface showed higher pLDDT values (50–80), supporting the interaction (Figure S7F). Fluorescence polarization assays showed that Gam blocks KwaB binding to both ssDNA and dsDNA, confirming competitive inhibition (Figure 7C).

Thus, Gam mimics DNA to bind KwaB and block its effector function.

Co-occurrence of Kiwa and RecBCD enables phage defense in the presence of Gam

The Lambda Gam protein inhibits the bacterial RecBCD complex by binding RecB.[48] RecBCD is essential for degrading phage DNA[49,50] and supports other defenses like CRISPR-Cas[51] and prokaryotic Argonaute.[52] Since RecBCD is present in our assay strains, we hypothesized that competition between RecBCD and Kiwa for Gam binding may limit Gam's ability to fully inhibit Kiwa.

To investigate this, we infected Kiwa- and Gam-expressing ΔRecB and $RecB^+$ cells with T4. In $RecB^+$ cells, Gam only partially inhibited Kiwa, but in ΔRecB, Kiwa was fully suppressed (Figure 7D), indicating that RecBCD partially buffers Gam inhibition of Kiwa.

We confirmed this using a T4Δgp2 mutant, which lacks the DNA-end-protecting protein gp2 and is thus vulnerable to RecBCD.[53] Kiwa and RecBCD each restricted T4Δgp2 in $RecB^+$ cells, and Gam could not inhibit Kiwa efficiently. But in ΔRecB cells, Gam fully suppressed Kiwa defense (Figure 7E). Thus, it appears that Gam availability is limited, and RecBCD acts as a competing target that safeguards Kiwa function. The inhibitory effects of Gam on RecBCD and Kiwa are structurally exclusive, and a single Gam dimer cannot inhibit both simultaneously (Figure S7G).

We next analyzed this competition in a more native setting. As shown earlier, Kiwa reduces Lambda infectivity by ~2 logs in $RecB^+$ cells but only by ~0.5 logs in ΔRecB cells, suggesting more free Gam is available in the absence of RecBCD (Figure S7A). Conversely, a Gam-inactive Lambda variant[47] was strongly inhibited (~5 logs) by Kiwa regardless of the RecB status (Figure S7A). We next tested whether high Gam levels could saturate both defenses by complementing the Gam-inactive Lambda variant with plasmid-expressed Gam. In both $RecB^+$ and ΔRecB cells, plasmid-expressed Gam suppressed Kiwa more effectively than phage-encoded Gam (Figure S7H), likely due to stronger expression and to the presence of Gam before phage infection, allowing pre-emptive inhibition of both defenses.

Thus, although RecBCD and Kiwa are individually susceptible to Gam, their co-occurrence creates a buffering effect, allowing one system to function when the other is inhibited.

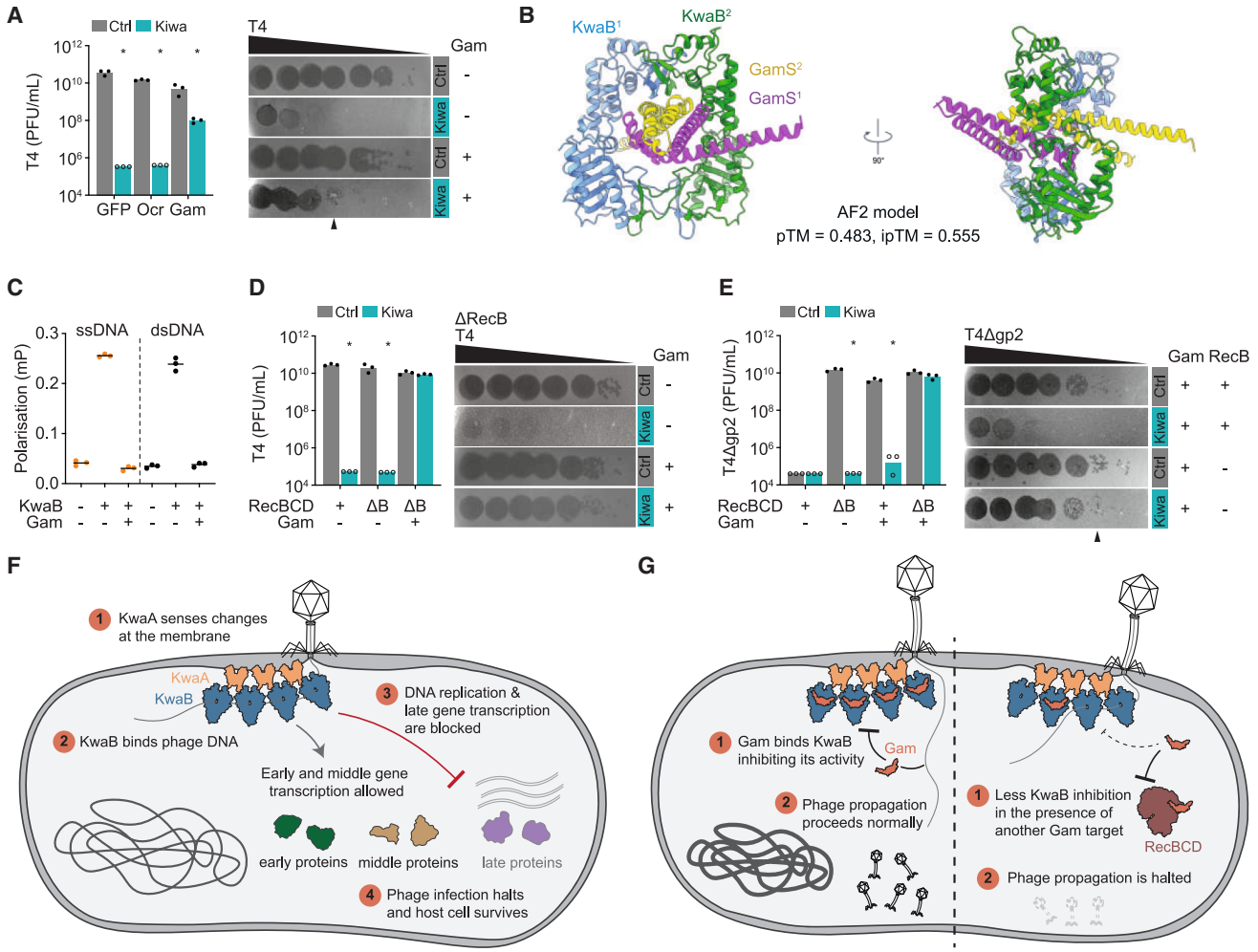

Figure 7. Kiwa is antagonized by phage-encoded DNA-mimic protein Gam

(A) Effect of T7 Ocr and Lambda Gam expression on Kiwa defense against T4. Left: phage titers (PFU/mL) on control (YFP) or Kiwa strains expressing the indicated proteins. *$p < 0.05$ (two-way ANOVA). Bars show means ($n = 3$) with individual data points, and open points indicate undetectable individual plaques (value of 1 assigned). Right: representative spot assays showing dilutions at which plaques appear in Kiwa Gam+ but not Kiwa Gam−.

(B) Two views of AlphaFold2 (AF2) model of KwaB dimer (blue and green) complexed with GamS dimer (magenta and yellow).

(C) Fluorescence anisotropy binding of KwaB to 20 bp ssDNA or dsDNA in the presence or absence of Gam. Data shown as polarization (mP, $n = 3$) using 1 μM KwaB monomer, 50 nM DNA, and 10 μM Gam.

(D) Effect of RecB subunit deletion and Gam expression on Kiwa defense against T4. *$p < 0.05$ (two-way ANOVA). Left: bars show means ($n = 3$) with individual points, and open points indicate undetectable individual plaques. Right: representative spot assays on ΔRecB control and Kiwa strains with or without Gam.

(E) Effect of ΔRecB and Gam expression on Kiwa defense against T4Δgp2. *$p < 0.05$ (two-way ANOVA). Left: bars show means ($n = 3$) with individual data points. Right: representative spot assays on control or Kiwa strains with or without Gam or RecB.

(F) Model: the Kiwa supercomplex localizes to the infection site, sensing perturbations caused by phage attachment and/or DNA ejection. After phage DNA entry, KwaB binds phage DNA, blocks replication and late transcription, and allows cell survival.

(G) Gam inhibits KwaB by mimicking DNA and occupying its binding site (left). In the presence of RecBCD, Gam availability to KwaB is reduced, partially restoring Kiwa activity (right).

See also Figure S7.

DISCUSSION

We described the structure and mechanism of Kiwa, revealing how it detects infection and halts phage replication without harming the host. Kiwa forms a membrane-embedded KwaAB supercomplex, where the transmembrane protein KwaA acts as a sensor and the cytoplasmic protein KwaB as a DNA-binding effector. Upon phage infection, this complex localizes to phage attachment sites and blocks phage DNA replication and late gene transcription (Figure 7F).

Our data indicate that KwaA senses infection at the membrane, likely in response to physical changes triggered by phage attachment or DNA ejection. The periplasmic loop PL1 of KwaA is a candidate sensory element, resembling the flexible extracellular loops of eukaryotic tetraspanins that detect viral ligands.[38,40] Although the specific trigger remains unknown, the

formation of KwaAB foci at phage attachment sites before (full) DNA ejection supports membrane-localized activation, a theme shared with other prokaryotic and eukaryotic sensors of infection and structural stress.[54]

KwaB binds DNA non-specifically *in vitro* and is essential for defense but is inactive without KwaA, suggesting that KwaA both localizes and activates KwaB, likely through conformational changes or induced supercomplex assembly. Our cryo-EM structure defines the KwaA-KwaB interface, supporting a model where sensing by KwaA transmits activation signals to KwaB through direct contact. The infection-dependent clustering of KwaAB indicates that activation involves regulated supercomplex formation at the infection site, likely ensuring a targeted response without host toxicity.

Our structural and modeling data indicate that phage-encoded DNA-mimic protein Gam[55] inhibits KwaB by occupying its DNA-interaction site, inducing a similar conformational change, and acting as a dominant negative inhibitor. Although both Kiwa and RecBCD are susceptible to Gam, their co-occurrence in *E. coli* provides resilience (Figure 7G). This implies that Gam availability is limiting, and RecBCD effectively buffers its action on Kiwa. This interplay highlights the adaptive advantage of defense redundancy. Coexisting defenses reduce the chance that a single phage inhibitor can entirely bypass host immunity, a pattern also observed in other defense combinations.[56] Although phages benefit from multipurpose inhibitors like DNA mimics,[44,57–59] hosts counter with layered defenses, such as RecBCD and Kiwa, to maintain an effective barrier.

In summary, Kiwa is a non-suicidal, membrane-activated defense that halts phage replication and transcription through a DNA-binding effector controlled by structure coordination. Our findings support a view of prokaryotic immunity as an interconnected, multilayered network, leveraging redundancy and versatility to counter fast-evolving phage threats.

Limitations of the study

Important aspects of the Kiwa mechanism remain unresolved. Our findings suggest membrane-localized activation, likely triggered by structural changes during phage attachment, but the molecular trigger and how KwaA senses it are unclear. The proposed role of KwaA periplasmic loops remains hypothetical and will require direct testing (e.g., loop-swapping), mindful of structural context and supercomplex integrity. The contribution of phage tail fibers to activation is not fully understood either but may help define the trigger sensed by KwaA.

We show that KwaB binding to phage DNA disrupts replication and late transcription, but how this occurs mechanistically, whether by stalling forks, blocking RNAP, or involving host factors, remains to be determined. The effect of phage-encoded RNAP inhibitors on KwaB activity suggests modulation at the effector stage, but the precise mechanism is unknown. Additionally, KwaB-DNA-binding is non-toxic in the absence of KwaA, implying regulation by structural coordination or additional factors that remain to be identified.

Finally, although Gam inhibits KwaB via DNA mimicry, we were unable to resolve the full KwaAB-Gam complex, limiting insight into the precise inhibitory mechanism. Our data indicate that Kiwa and RecBCD provide overlapping protection against such inhibitors, but the extent and dynamics of this redundancy across bacterial species and environmental niches remain open questions for future study.

RESOURCE AVAILABILITY

Lead contact

Further information and requests for resources and reagents should be directed to and will be fulfilled by the lead contact, Franklin L. Nobrega (f.nobrega@soton.ac.uk).

Materials availability

All unique bacterial strains, phages, and plasmids generated in this study are available from the lead contact without restriction.

Data and code availability

- Raw data have been deposited at Figshare at https://doi.org/10.6084/m9.figshare.21652433.v1, https://doi.org/10.6084/m9.figshare.29025803, and https://doi.org/10.6084/m9.figshare.29029154, Protein Data Base (PDB: 9MRG, PDB: 9MRR, PDB: 9MRX, PDB: 9O01, PDB: 9MTN, and PDB: 9NYU), and the Electron Microscopy Data Bank (EMDB: EMD-48556, EMDB: EMD-48562, EMDB: EMD-48564, and EMDB: EMD-49973) and are publicly available as of the date of publication.
- This paper does not report original code.
- Any additional information required to reanalyze the data reported in this paper is available from the lead contact upon request.

ACKNOWLEDGMENTS

We thank Rotem Sorek (Weizmann Institute of Science) for the Lambda Gam mutant and Ian Molineux (University of Texas) for T4Δgp2. We thank You Yu (Zhejiang University-University of Edinburgh Institute) and J. De La Cruz (MSK) for assistance with cryo-EM data collection and Lyuqin Zheng (MSK) for discussions on structural analysis. We thank the Imaging and Microscopy Centre (IMC) at the University of Southampton. This work was supported by Royal Society grant RGS\R2\222312 to F.L.N.; Welch Foundation grant F-1938 and National Institutes of Health R35GM138348 to D.W.T.; Wessex Medical Research Innovation grant AE06 to T.A.; and NIH grant GM145888 and Maloris Foundation and Memorial Sloan-Kettering Core grant (P30-CA008748) to D.J.P. In addition to MSKCC cryo-EM resources, some of this work was performed at the National Center for CryoEM Access and Training (NCCAT) and the Simons Electron Microscopy Center located at the New York Structural Biology Center, supported by the NIH Common Fund Transformative High Resolution Cryo-Electron Microscopy program (U24 GM129539) and Simons Foundation (SF349247) and NY State Assembly grants. This research used NSLS-II MX X-ray User Resources (FMX) of the National Synchrotron Light Source II, operated for the DOE Office of Science by Brookhaven National Laboratory under contract no. DE-SC0012704. The Center for BioMolecular Structure (CBMS) is primarily supported by the NIH, the National Institute of General Medical Sciences (NIGMS) through a Center Core P30 Grant (P30GM133893), and by the DOE Office of Biological and Environmental Research (KP1605010). R.K. and E.V.K. are supported by the Intramural Research Program of the NIH (National Library of Medicine).

AUTHOR CONTRIBUTIONS

Conceptualization, F.L.N.; methodology, Z.Z., T.C.T., Y.W., R.K., D.K., E.V.K., D.J.P., and F.L.N.; formal analysis, T.C.T., T.A., R.K., F.L.N., J.P.K.B., and D.W.T.; investigation, Z.Z., T.C.T., Y.W., J.C.R., M.T., T.A., A.N., R.M., and J.P.K.B.; visualization, Z.Z., T.C.T., T.A., Y.W., R.K., and T.A.; data curation, T.C.T., Y.W., and F.L.N.; writing – original draft, Z.Z., T.C.T., Y.W., R.K., E.V.K., D.J.P., and F.L.N.; writing – review and editing, D.P., E.V.K., and F.L.N.; resources, D.K., D.W.T., D.J.P., E.V.K., and F.L.N.; funding acquisition, D.P., and F.L.N.

DECLARATION OF INTERESTS

The authors declare no competing interests.

STAR★METHODS

Detailed methods are provided in the online version of this paper and include the following:

- KEY RESOURCES TABLE
- EXPERIMENTAL MODEL AND STUDY PARTICIPANT DETAILS
  - Bacterial strains and phages
- METHOD DETAILS
  - Plasmid and strain construction
  - Plaque assays
  - Time post infection assays
  - Conjugation assays
  - DNA replication assay
  - Bacterial two-hybrid assay
  - RecBCD mutant assays
  - Isolation and sequencing of escape phages
  - Amplification of mutant phages in cells expressing wild type tail fibres
  - Protein expression and purification
  - KwaA expression and purification
  - KwaB expression and purification
  - KwaAB expression and purification
  - Cryo-EM sample preparation and data collection
  - Cryo-EM data processing
  - Crystallisation and data collection
  - Model building, structure refinement, and visualisation
  - Modelling the KwaAB supercomplex
  - AlphaFold prediction and visualisation
  - KwaB mutants' expression and purification
  - Mass photometry
  - Electrophoretic mobility shift assay
  - *In vitro* nuclease activity
  - Fluorescence anisotropy binding assays
  - Pull-down assay for GamS and KwaB
  - Western blot
  - Confocal microscopy
  - RNAseq
  - Bioinformatic analysis
- QUANTIFICATION AND STATISTICAL ANALYSIS

SUPPLEMENTAL INFORMATION

Supplemental information can be found online at https://doi.org/10.1016/j.cell.2025.07.002.

Received: February 1, 2025
Revised: May 13, 2025
Accepted: July 2, 2025
Published: July 28, 2025

REFERENCES

1. Georjon, H., and Bernheim, A. (2023). The highly diverse antiphage defence systems of bacteria. Nat. Rev. Microbiol. *21*, 686–700. https://doi.org/10.1038/s41579-023-00934-x.
2. Egido, J.E., Costa, A.R., Aparicio-Maldonado, C., Haas, P.-J., and Brouns, S.J.J. (2022). Mechanisms and clinical importance of bacteriophage resistance. FEMS Microbiol. Rev. *46*, fuab048. https://doi.org/10.1093/femsre/fuab048.
3. Agapov, A., Baker, K.S., Bedekar, P., Bhatia, R.P., Blower, T.R., Brockhurst, M.A., Brown, C., Chong, C.E., Fothergill, J.L., Graham, S., et al. (2024). Multi-layered genome defences in bacteria. Curr. Opin. Microbiol. *78*, 102436. https://doi.org/10.1016/j.mib.2024.102436.
4. Anzalone, A.V., Koblan, L.W., and Liu, D.R. (2020). Genome editing with CRISPR–Cas nucleases, base editors, transposases and prime editors. Nat. Biotechnol. *38*, 824–844. https://doi.org/10.1038/s41587-020-0561-9.
5. Millman, A., Melamed, S., Leavitt, A., Doron, S., Bernheim, A., Hör, J., Garb, J., Bechon, N., Brandis, A., Lopatina, A., et al. (2022). An expanded arsenal of immune systems that protect bacteria from phages. Cell Host Microbe *30*, 1556–1569. https://doi.org/10.1016/j.chom.2022.09.017.
6. Doron, S., Melamed, S., Ofir, G., Leavitt, A., Lopatina, A., Keren, M., Amitai, G., and Sorek, R. (2018). Systematic discovery of antiphage defense systems in the microbial pangenome. Science *359*, eaar4120. https://doi.org/10.1126/science.aar4120.
7. Ofir, G., Melamed, S., Sberro, H., Mukamel, Z., Silverman, S., Yaakov, G., Doron, S., and Sorek, R. (2018). DISARM is a widespread bacterial defence system with broad anti-phage activities. Nat. Microbiol. *3*, 90–98. https://doi.org/10.1038/s41564-017-0051-0.
8. Goldfarb, T., Sberro, H., Weinstock, E., Cohen, O., Doron, S., Charpak-Amikam, Y., Afik, S., Ofir, G., and Sorek, R. (2015). BREX is a novel phage resistance system widespread in microbial genomes. EMBO J. *34*, 169–183. https://doi.org/10.15252/embj.201489455.
9. Gao, L., Altae-Tran, H., Böhning, F., Makarova, K.S., Segel, M., Schmid-Burgk, J.L., Koob, J., Wolf, Y.I., Koonin, E.V., and Zhang, F. (2020). Diverse enzymatic activities mediate antiviral immunity in prokaryotes. Science *369*, 1077–1084. https://doi.org/10.1126/science.aba0372.
10. Owen, S.V., Wenner, N., Dulberger, C.L., Rodwell, E.V., Bowers-Barnard, A., Quinones-Olvera, N., Rigden, D.J., Rubin, E.J., Garner, E.C., Baym, M., and Hinton, J.C.D. (2021). Prophages encode phage-defense systems with cognate self-immunity. Cell Host Microbe *29*, 1620–1633. https://doi.org/10.1016/j.chom.2021.09.002.
11. Rousset, F., Depardieu, F., Miele, S., Dowding, J., Laval, A.-L., Lieberman, E., Garry, D., Rocha, E.P.C., Bernheim, A., and Bikard, D. (2022). Phages and their satellites encode hotspots of antiviral systems. Cell Host Microbe *30*, 740–753. https://doi.org/10.1016/j.chom.2022.02.018.
12. Vassallo, C.N., Doering, C.R., Littlehale, M.L., Teodoro, G.I.C., and Laub, M.T. (2022). A functional selection reveals previously undetected anti-phage defence systems in the E. coli pangenome. Nat. Microbiol. *7*, 1568–1579. https://doi.org/10.1038/s41564-022-01219-4.
13. Payne, L.J., Todeschini, T.C., Wu, Y., Perry, B.J., Ronson, C.W., Fineran, P.C., Nobrega, F.L., and Jackson, S.A. (2021). Identification and classification of antiviral defence systems in bacteria and archaea with PADLOC reveals new system types. Nucleic Acids Res. *49*, 10868–10878. https://doi.org/10.1093/nar/gkab883.
14. Payne, L.J., Meaden, S., Mestre, M.R., Palmer, C., Toro, N., Fineran, P.C., and Jackson, S.A. (2022). PADLOC: a web server for the identification of antiviral defence systems in microbial genomes. Nucleic Acids Res. *50*, W541–W550. https://doi.org/10.1093/nar/gkac400.
15. Galperin, M.Y., Vera Alvarez, R., Karamycheva, S., Makarova, K.S., Wolf, Y.I., Landsman, D., and Koonin, E.V. (2025). COG database update 2024. Nucleic Acids Res. *53*, D356–D363. https://doi.org/10.1093/nar/gkae983.
16. Parks, D.H., Chuvochina, M., Rinke, C., Mussig, A.J., Chaumeil, P.-A., and Hugenholtz, P. (2022). GTDB: an ongoing census of bacterial and archaeal diversity through a phylogenetically consistent, rank normalized and complete genome-based taxonomy. Nucleic Acids Res. *50*, D785–D794. https://doi.org/10.1093/nar/gkab776.
17. Ofir, G., Herbst, E., Baroz, M., Cohen, D., Millman, A., Doron, S., Tal, N., Malheiro, D.B.A., Malitsky, S., Amitai, G., and Sorek, R. (2021). Antiviral activity of bacterial TIR domains via immune signalling molecules. Nature *600*, 116–120. https://doi.org/10.1038/s41586-021-04098-7.
18. Duncan-Lowey, B., McNamara-Bordewick, N.K., Tal, N., Sorek, R., and Kranzusch, P.J. (2021). Effector-mediated membrane disruption controls

cell death in CBASS antiphage defense. Mol. Cell *81*, 5039–5051. https://doi.org/10.1016/j.molcel.2021.10.020.

19. Mount, J., Maksaev, G., Summers, B.T., Fitzpatrick, J.A.J., and Yuan, P. (2022). Structural basis for mechanotransduction in a potassium-dependent mechanosensitive ion channel. Nat. Commun. *13*, 6904. https://doi.org/10.1038/s41467-022-34737-0.
20. Lopatina, A., Tal, N., and Sorek, R. (2020). Abortive Infection: Bacterial Suicide as an Antiviral Immune Strategy. Annu. Rev. Virol. *7*, 371–384. https://doi.org/10.1146/annurev-virology-011620-040628.
21. Aframian, N., and Eldar, A. (2023). Abortive infection antiphage defense systems: separating mechanism and phenotype. Trends Microbiol. *31*, 1003–1012. https://doi.org/10.1016/j.tim.2023.05.002.
22. Kutter, E., Bryan, D., Ray, G., Brewster, E., Blasdel, B., and Guttman, B. (2018). From Host to Phage Metabolism: Hot Tales of Phage T4's Takeover of E. coli. Viruses *10*, 387. https://doi.org/10.3390/v10070387.
23. Michel, B., Boubakri, H., Baharoglu, Z., LeMasson, M., and Lestini, R. (2007). Recombination proteins and rescue of arrested replication forks. DNA Repair *6*, 967–980. https://doi.org/10.1016/j.dnarep.2007.02.016.
24. Mosig, G. (1998). Recombination and recombination-dependent dna replication in bacteriophage T4. Annu. Rev. Genet. *32*, 379–413. https://doi.org/10.1146/annurev.genet.32.1.379.
25. Formosa, T., and Alberts, B.M. (1986). DNA synthesis dependent on genetic recombination: Characterization of a reaction catalyzed by purified bacteriophage T4 proteins. Cell *47*, 793–806. https://doi.org/10.1016/0092-8674(86)90522-2.
26. Kreuzer, K.N., and Brister, J.R. (2010). Initiation of bacteriophage T4 DNA replication and replication fork dynamics: a review in the Virology Journal series on bacteriophage T4 and its relatives. Virol. J. *7*, 358. https://doi.org/10.1186/1743-422X-7-358.
27. Yuan, Q., Xie, J., Xie, J., Zhao, H., and Yang, Y. (2023). Fast and accurate protein function prediction from sequence through pretrained language model and homology-based label diffusion. Brief. Bioinform. *24*, bbad117. https://doi.org/10.1093/bib/bbad117.
28. Hellman, L.M., and Fried, M.G. (2007). Electrophoretic mobility shift assay (EMSA) for detecting protein–nucleic acid interactions. Nat. Protoc. *2*, 1849–1861. https://doi.org/10.1038/nprot.2007.249.
29. Edgar, R., Rokney, A., Feeney, M., Semsey, S., Kessel, M., Goldberg, M. B., Adhya, S., and Oppenheim, A.B. (2008). Bacteriophage infection is targeted to cellular poles. Mol. Microbiol. *68*, 1107–1116. https://doi.org/10.1111/j.1365-2958.2008.06205.x.
30. Tabib-Salazar, A., Liu, B., Barker, D., Burchell, L., Qimron, U., Matthews, S.J., and Wigneshweraraj, S. (2018). T7 phage factor required for managing RpoS in Escherichia coli. Proc. Natl. Acad. Sci. USA *115*, E5353–E5362. https://doi.org/10.1073/pnas.1800429115.
31. Tabib-Salazar, A., Liu, B., Shadrin, A., Burchell, L., Wang, Z., Wang, Z., Goren, M.G., Yosef, I., Qimron, U., Severinov, K., et al. (2017). Full shutoff of Escherichia coli RNA-polymerase by T7 phage requires a small phage-encoded DNA-binding protein. Nucleic Acids Res. *45*, 7697–7707. https://doi.org/10.1093/nar/gkx370.
32. Zhang, T., Cepauskas, A., Nadieina, A., Thureau, A., Coppieters 't Wallant, K., Martens, C., Lim, D.C., Garcia-Pino, A., and Laub, M.T. (2024). A bacterial immunity protein directly senses two disparate phage proteins. Nature *635*, 728–735. https://doi.org/10.1038/s41586-024-08039-y.
33. Gao, L.A., Wilkinson, M.E., Strecker, J., Makarova, K.S., Macrae, R.K., Koonin, E.V., and Zhang, F. (2022). Prokaryotic innate immunity through pattern recognition of conserved viral proteins. Science *377*, eabm4096. https://doi.org/10.1126/science.abm4096.
34. Hallman, M., Rämet, M., and Ezekowitz, R.A. (2001). Toll-like Receptors as Sensors of Pathogens. Pediatr. Res. *50*, 315–321. https://doi.org/10.1203/00006450-200109000-00004.
35. Cheung, J., and Hendrickson, W.A. (2010). Sensor domains of two-component regulatory systems. Curr. Opin. Microbiol. *13*, 116–123. https://doi.org/10.1016/j.mib.2010.01.016.
36. Padmanabhan, M., Cournoyer, P., and Dinesh-Kumar, S.P. (2009). The leucine-rich repeat domain in plant innate immunity: a wealth of possibilities. Cell. Microbiol. *11*, 191–198. https://doi.org/10.1111/j.1462-5822.2008.01260.x.
37. Bailey, C.C., Zhong, G., Huang, I.-C., and Farzan, M. (2014). IFITM-Family Proteins: The Cell's First Line of Antiviral Defense. Annu. Rev. Virol. *1*, 261–283. https://doi.org/10.1146/annurev-virology-031413-085537.
38. Lang, T., and Hochheimer, N. (2020). Tetraspanins. Curr. Biol. *30*, R204–R206. https://doi.org/10.1016/j.cub.2020.01.007.
39. Susa, K.J., Kruse, A.C., and Blacklow, S.C. (2024). Tetraspanins: structure, dynamics, and principles of partner-protein recognition. Trends Cell Biol. *34*, 509–522. https://doi.org/10.1016/j.tcb.2023.09.003.
40. Florin, L., and Lang, T. (2018). Tetraspanin Assemblies in Virus Infection. Front. Immunol. *9*, 1140. https://doi.org/10.3389/fimmu.2018.01140.
41. Mayo-Muñoz, D., Pinilla-Redondo, R., Camara-Wilpert, S., Birkholz, N., and Fineran, P.C. (2024). Inhibitors of bacterial immune systems: discovery, mechanisms and applications. Nat. Rev. Genet. *25*, 237–254. https://doi.org/10.1038/s41576-023-00676-9.
42. Yirmiya, E., Leavitt, A., Lu, A., Ragucci, A.E., Avraham, C., Osterman, I., Garb, J., Antine, S.P., Mooney, S.E., Hobbs, S.J., et al. (2024). Phages overcome bacterial immunity via diverse anti-defence proteins. Nature *625*, 352–359. https://doi.org/10.1038/s41586-023-06869-w.
43. Shin, J., Jiang, F., Liu, J.-J., Bray, N.L., Rauch, B.J., Baik, S.H., Nogales, E., Bondy-Denomy, J., Corn, J.E., and Doudna, J.A. (2017). Disabling Cas9 by an anti-CRISPR DNA mimic. Sci. Adv. *3*, e1701620. https://doi.org/10.1126/sciadv.1701620.
44. Isaev, A., Drobiazko, A., Sierro, N., Gordeeva, J., Yosef, I., Qimron, U., Ivanov, N.V., and Severinov, K. (2020). Phage T7 DNA mimic protein Ocr is a potent inhibitor of BREX defence. Nucleic Acids Res. *48*, 5397–5406. https://doi.org/10.1093/nar/gkaa290.
45. Krüger, D.H., and Schroeder, C. (1981). Bacteriophage T3 and bacteriophage T7 virus-host cell interactions. Microbiol. Rev. *45*, 9–51. https://doi.org/10.1128/mr.45.1.9-51.1981.
46. Sakaki, Y., Karu, A.E., Linn, S., and Echols, H. (1973). Purification and Properties of the γ-Protein Specified by Bacteriophage λ: An Inhibitor of the Host RecBC Recombination Enzyme. Proc. Natl. Acad. Sci. USA *70*, 2215–2219. https://doi.org/10.1073/pnas.70.8.2215.
47. Millman, A., Bernheim, A., Stokar-Avihail, A., Fedorenko, T., Voichek, M., Leavitt, A., Oppenheimer-Shaanan, Y., and Sorek, R. (2020). Bacterial Retrons Function In Anti-Phage Defense. Cell *183*, 1551–1561. https://doi.org/10.1016/j.cell.2020.09.065.
48. Marsić, N., Roje, S., Stojiljković, I., Salaj-Smic, E., and Trgovcević, Z. (1993). In vivo studies on the interaction of RecBCD enzyme and lambda Gam protein. J. Bacteriol. *175*, 4738–4743. https://doi.org/10.1128/jb.175.15.4738-4743.1993.
49. Dillingham, M.S., and Kowalczykowski, S.C. (2008). RecBCD Enzyme and the Repair of Double-Stranded DNA Breaks. Microbiol. Mol. Biol. Rev. *72*, 642–671. https://doi.org/10.1128/MMBR.00020-08.
50. Cheng, K., Wilkinson, M., Chaban, Y., and Wigley, D.B. (2020). A conformational switch in response to Chi converts RecBCD from phage destruction to DNA repair. Nat. Struct. Mol. Biol. *27*, 71–77. https://doi.org/10.1038/s41594-019-0355-2.
51. Levy, A., Goren, M.G., Yosef, I., Auster, O., Manor, M., Amitai, G., Edgar, R., Qimron, U., and Sorek, R. (2015). CRISPR adaptation biases explain preference for acquisition of foreign DNA. Nature *520*, 505–510. https://doi.org/10.1038/nature14302.
52. Kuzmenko, A., Oguienko, A., Esyunina, D., Yudin, D., Petrova, M., Kudinova, A., Maslova, O., Ninova, M., Ryazansky, S., Leach, D., et al. (2020). DNA targeting and interference by a bacterial Argonaute nuclease. Nature *587*, 632–637. https://doi.org/10.1038/s41586-020-2605-1.
53. Lipinska, B., Rao, A.S., Bolten, B.M., Balakrishnan, R., and Goldberg, E.B. (1989). Cloning and identification of bacteriophage T4 gene 2 product gp2

and action of gp2 on infecting DNA in vivo. J. Bacteriol. *171*, 488–497. https://doi.org/10.1128/jb.171.1.488-497.1989.

54. Xie, P., Zhang, H., Qin, Y., Xiong, H., Shi, C., and Zhou, Z. (2023). Membrane Proteins and Membrane Curvature: Mutual Interactions and a Perspective on Disease Treatments. Biomolecules *13*, 1772. https://doi.org/10.3390/biom13121772.

55. Wilkinson, M., Troman, L., Wan Nur Ismah, W.A., Chaban, Y., Avison, M.B., Dillingham, M.S., and Wigley, D.B. (2016). Structural basis for the inhibition of RecBCD by Gam and its synergistic antibacterial effect with quinolones. eLife *5*, e22963. https://doi.org/10.7554/eLife.22963.

56. Silas, S., Carion, H., Makarova, K.S., Laderman, E.S., Todeschini, T., Kumar, P., Johnson, M., Bocek, M., Nobrega, F.L., Koonin, E.V., and Bondy-Denomy, J. (2025). Activation of bacterial programmed cell death by phage inhibitors of host immunity. Mol. Cell *85*, 1838–1851. https://doi.org/10.1016/j.molcel.2025.04.010.

57. Kudryavtseva, A.A., Cséfalvay, E., Gnuchikh, E.Y., Yanovskaya, D.D., Skutel, M.A., Isaev, A.B., Bazhenov, S.V., Utkina, A.A., and Manukhov, I. V. (2023). Broadness and specificity: ArdB, ArdA, and Ocr against various restriction-modification systems. Front. Microbiol. *14*, 1133144. https://doi.org/10.3389/fmicb.2023.1133144.

58. Osterman, I., Samra, H., Rousset, F., Loseva, E., Itkin, M., Malitsky, S., Yirmiya, E., Millman, A., and Sorek, R. (2024). Phages reconstitute NAD^+ to counter bacterial immunity. Nature *634*, 1160–1167. https://doi.org/10.1038/s41586-024-07986-w.

59. Jiang, S., Chen, C., Huang, W., He, Y., Du, X., Wang, Y., Ou, H., Deng, Z., Xu, C., Jiang, L., et al. (2024). A widespread phage-encoded kinase enables evasion of multiple host antiphage defence systems. Nat. Microbiol. *9*, 3226–3239. https://doi.org/10.1038/s41564-024-01851-2.

60. Jumper, J., Evans, R., Pritzel, A., Green, T., Figurnov, M., Ronneberger, O., Tunyasuvunakool, K., Bates, R., Žídek, A., Potapenko, A., et al. (2021). Highly accurate protein structure prediction with AlphaFold. Nature *596*, 583–589. https://doi.org/10.1038/s41586-021-03819-2.

61. Cianfrocco, M.A., Wong-Barnum, M., Youn, C., Wagner, R., and Leschziner, A. (2017). COSMIC2: A Science Gateway for Cryo-Electron Microscopy Structure Determination. In Practice and Experience in Advanced Research Computing 2017: Sustainability, Success and Impact (PEARC '17) (Association for Computing Machinery), pp. 1–5. https://doi.org/10.1145/3093338.3093390.

62. Bushnell, B., Rood, J., and Singer, E. (2017). BBMerge – Accurate paired shotgun read merging via overlap. PLoS One *12*, e0185056. https://doi.org/10.1371/journal.pone.0185056.

63. Deatherage, D.E., and Barrick, J.E. (2014). Identification of Mutations in Laboratory-Evolved Microbes from Next-Generation Sequencing Data Using breseq. In Engineering and Analyzing Multicellular Systems: Methods and Protocols, L. Sun and W. Shou, eds. (Springer), pp. 165–188. https://doi.org/10.1007/978-1-4939-0554-6_12.

64. Meng, E.C., Goddard, T.D., Pettersen, E.F., Couch, G.S., Pearson, Z.J., Morris, J.H., and Ferrin, T.E. (2023). UCSF ChimeraX: Tools for structure building and analysis. Protein Sci. *32*, e4792. https://doi.org/10.1002/pro.4792.

65. Steenwyk, J.L., Buida, T.J., III, Li, Y., Shen, X.-X., and Rokas, A. (2020). ClipKIT: A multiple sequence alignment trimming software for accurate phylogenomic inference. PLoS Biol. *18*, e3001007. https://doi.org/10.1371/journal.pbio.3001007.

66. Sievers, F., Wilm, A., Dineen, D., Gibson, T.J., Karplus, K., Li, W., Lopez, R., McWilliam, H., Remmert, M., Söding, J., et al. (2011). Fast, scalable generation of high-quality protein multiple sequence alignments using Clustal Omega. Mol. Syst. Biol. *7*, 539. https://doi.org/10.1038/msb.2011.75.

67. Emsley, P., Lohkamp, B., Scott, W.G., and Cowtan, K. (2010). Features and development of Coot. Acta Crystallogr. D Biol. Crystallogr. *66*, 486–501. https://doi.org/10.1107/S0907444910007493.

68. Punjani, A., Rubinstein, J.L., Fleet, D.J., and Brubaker, M.A. (2017). cryoSPARC: algorithms for rapid unsupervised cryo-EM structure determination. Nat. Methods *14*, 290–296. https://doi.org/10.1038/nmeth.4169.

69. Holm, L., and Laakso, L.M. (2016). Dali server update. Nucleic Acids Res. *44*, W351–W355. https://doi.org/10.1093/nar/gkw357.

70. Hallgren, J., Tsirigos, K.D., Pedersen, M.D., Almagro Armenteros, J.J., Marcatili, P., Nielsen, H., Krogh, A., and Winther, O. (2022). DeepTMHMM predicts alpha and beta transmembrane proteins using deep neural networks. Preprint at bioRxiv, 2022.2004.2008.487609. https://doi.org/10.1101/2022.04.08.487609.

71. Camargo, A.P., Roux, S., Schulz, F., Babinski, M., Xu, Y., Hu, B., Chain, P.S.G., Nayfach, S., and Kyrpides, N.C. (2024). Identification of mobile genetic elements with geNomad. Nat. Biotechnol. *42*, 1303–1312. https://doi.org/10.1038/s41587-023-01953-y.

72. Söding, J., Biegert, A., and Lupas, A.N. (2005). The HHpred interactive server for protein homology detection and structure prediction. Nucleic Acids Res. *33*, W244–W248. https://doi.org/10.1093/nar/gki408.

73. Kim, D., Paggi, J.M., Park, C., Bennett, C., and Salzberg, S.L. (2019). Graph-based genome alignment and genotyping with HISAT2 and HISAT-genotype. Nat. Biotechnol. *37*, 907–915. https://doi.org/10.1038/s41587-019-0201-4.

74. Minh, B.Q., Schmidt, H.A., Chernomor, O., Schrempf, D., Woodhams, M. D., von Haeseler, A., and Lanfear, R. (2020). IQ-TREE 2: New Models and Efficient Methods for Phylogenetic Inference in the Genomic Era. Mol. Biol. Evol. *37*, 1530–1534. https://doi.org/10.1093/molbev/msaa015.

75. Letunic, I., and Bork, P. (2019). Interactive Tree Of Life (iTOL) v4: recent updates and new developments. Nucleic Acids Res. *47*, W256–W259. https://doi.org/10.1093/nar/gkz239.

76. Li, H. (2018). Minimap2: pairwise alignment for nucleotide sequences. Bioinformatics *34*, 3094–3100. https://doi.org/10.1093/bioinformatics/bty191.

77. Mukherjee, S., and Zhang, Y. (2009). MM-align: a quick algorithm for aligning multiple-chain protein complex structures using iterative dynamic programming. Nucleic Acids Res. *37*, e83. https://doi.org/10.1093/nar/gkp318.

78. Steinegger, M., and Söding, J. (2017). MMseqs2 enables sensitive protein sequence searching for the analysis of massive data sets. Nat. Biotechnol. *35*, 1026–1028. https://doi.org/10.1038/nbt.3988.

79. Kalyaanamoorthy, S., Minh, B.Q., Wong, T.K.F., von Haeseler, A., and Jermiin, L.S. (2017). ModelFinder: fast model selection for accurate phylogenetic estimates. Nat. Methods *14*, 587–589. https://doi.org/10.1038/nmeth.4285.

80. Edgar, R.C. (2022). Muscle5: High-accuracy alignment ensembles enable unbiased assessments of sequence homology and phylogeny. Nat. Commun. *13*, 6968. https://doi.org/10.1038/s41467-022-34630-w.

81. McCoy, A.J., Grosse-Kunstleve, R.W., Adams, P.D., Winn, M.D., Storoni, L.C., and Read, R.J. (2007). Phaser crystallographic software. J. Appl. Crystallogr. *40*, 658–674. https://doi.org/10.1107/S0021889807021206.

82. Adams, P.D., Afonine, P.V., Bunkóczi, G., Chen, V.B., Davis, I.W., Echols, N., Headd, J.J., Hung, L.W., Kapral, G.J., Grosse-Kunstleve, R.W., et al. (2010). PHENIX: a comprehensive Python-based system for macromolecular structure solution. Acta Crystallogr. D Biol. Crystallogr. *66*, 213–221. https://doi.org/10.1107/S0907444909052925.

83. Li, W., O'Neill, K.R., Haft, D.H., DiCuccio, M., Chetvernin, V., Badretdin, A., Coulouris, G., Chitsaz, F., Derbyshire, M.K., Durkin, A.S., et al. (2021). RefSeq: expanding the Prokaryotic Genome Annotation Pipeline reach with protein family model curation. Nucleic Acids Res. *49*, D1020–D1028. https://doi.org/10.1093/nar/gkaa1105.

84. Omasits, U., Ahrens, C.H., Müller, S., and Wollscheid, B. (2014). Protter: interactive protein feature visualization and integration with experimental proteomic data. Bioinformatics *30*, 884–886. https://doi.org/10.1093/bioinformatics/btt607.

85. Mastronarde, D.N. (2005). Automated electron microscope tomography using robust prediction of specimen movements. J. Struct. Biol. *152*, 36–51. https://doi.org/10.1016/j.jsb.2005.07.007.

86. Vera Alvarez, R., Pongor, L.S., Mariño-Ramírez, L., and Landsman, D. (2019). TPMCalculator: one-step software to quantify mRNA abundance of genomic features. Bioinformatics *35*, 1960–1962. https://doi.org/10.1093/bioinformatics/bty896.

87. Banerjee, P., Eulenstein, O., and Friedberg, I. (2024). Discovering genomic islands in unannotated bacterial genomes using sequence embedding. Bioinform. Adv. *4*, vbae089. https://doi.org/10.1093/bioadv/vbae089.

88. Hoang, D.T., Chernomor, O., von Haeseler, A., Minh, B.Q., and Vinh, L.S. (2018). UFBoot2: Improving the Ultrafast Bootstrap Approximation. Mol. Biol. Evol. *35*, 518–522. https://doi.org/10.1093/molbev/msx281.

89. Baba, T., Ara, T., Hasegawa, M., Takai, Y., Okumura, Y., Baba, M., Datsenko, K.A., Tomita, M., Wanner, B.L., and Mori, H. (2006). Construction of Escherichia coli K-12 in-frame, single-gene knockout mutants: the Keio collection. Mol. Syst. Biol. *2*, 2006.0008. https://doi.org/10.1038/msb4100050.

90. Luong, T., Salabarria, A.-C., Edwards, R.A., and Roach, D.R. (2020). Standardized bacteriophage purification for personalized phage therapy. Nat. Protoc. *15*, 2867–2890. https://doi.org/10.1038/s41596-020-0346-0.

91. Pettersen, E.F., Goddard, T.D., Huang, C.C., Couch, G.S., Greenblatt, D. M., Meng, E.C., and Ferrin, T.E. (2004). UCSF Chimera–a visualization system for exploratory research and analysis. J. Comput. Chem. *25*, 1605–1612. https://doi.org/10.1002/jcc.20084.

92. Pettersen, E.F., Goddard, T.D., Huang, C.C., Meng, E.C., Couch, G.S., Croll, T.I., Morris, J.H., and Ferrin, T.E. (2021). UCSF ChimeraX: Structure visualization for researchers, educators, and developers. Protein Sci. *30*, 70–82. https://doi.org/10.1002/pro.3943.

93. Mirdita, M., Schütze, K., Moriwaki, Y., Heo, L., Ovchinnikov, S., and Steinegger, M. (2022). ColabFold: making protein folding accessible to all. Nat. Methods *19*, 679–682. https://doi.org/10.1038/s41592-022-01488-1.

94. Abramson, J., Adler, J., Dunger, J., Evans, R., Green, T., Pritzel, A., Ronneberger, O., Willmore, L., Ballard, A.J., Bambrick, J., et al. (2024). Accurate structure prediction of biomolecular interactions with AlphaFold 3. Nature *630*, 493–500. https://doi.org/10.1038/s41586-024-07487-w.

STAR★METHODS

KEY RESOURCES TABLE

REAGENT or RESOURCE	SOURCE	IDENTIFIER
Bacterial and virus strains		
All bacterial strains and bacteriophages are listed and described in Table S5	N/A	N/A
Chemicals, peptides, and recombinant proteins		
3x Flag tag peptide	Thermo Fisher Scientific	Cat# PIA36805
5- bromo-4-chloro-3-indolyl-β-D-galactopyranoside (X-Gal)	Thermo Fisher Scientific	Cat# B1690
6% DNA Retardation Gel	Invitrogen	Cat# EC63655BOX
Agar	Formedium	Cat# AGA04
Agarose	Melford	Cat# A20090
Ampicillin	Melford	Cat# A40040-10.0
Anti-6His tag	Invitrogen	Cat# MA1-21315-HRP, RRID: AB_2536989
Anti-FLAG M2 affinity gel	Sigma Aldrich	Cat# A2220, RRID: AB_2039163
Arabinose	Melford	Cat# A51000-100.0
Adenosine 5′-Triphosphate	New England Biolabs	Cat# P0756S
β-mercaptoethanol	Thermo Fisher Scientific	Cat# PI35602
Blotting Grade Blocker Non Fat Dry Milk	Bio-Rad	Cat# 1706404XTU
BSA protein standard	Sigma Aldrich	Cat# P0834
Chloramphenicol	Acros Organics	Cat# A0414716
Chloroform	Thermo Fisher Scientific	Cat# J67241.AP
Cholesteryl hemisuccinate (CHS)	Sigma Aldrich	Cat# C6512
cOmplete EDTA-free protease inhibitor	Sigma Aldrich	Cat# 11873580001
Dithiothreitol (DTT)	New England Biolabs	Cat# 7016L
DNA loading dye (with EDTA)	New England Biolabs	Cat# B7024S
DNase I	Sigma Aldrich	Cat# DN25
Ethylenediamine tetraacetic acid (EDTA)	Thermo Fisher Scientific	Cat# A10713.36
FM4-64 dye	Thermo Fisher Scientific	Cat# T13320
NEBExpress® GamS Nuclease Inhibitor	New England Biolabs	Cat# P0774S
Gentamycin	Melford	Cat# G38000-5.0
GroEL antibody	Fisher Scientific	Cat# NB018822, RRID: AB_2039163
Goat anti-mouse IgG	Millipore Sigma	Cat# AP124P, RRID: AB_90456
UltrAuFoil® R 1.2/1.3 300 Mesh Gold Grid	Sigma-Aldrich	Cat# Q350AR13A
Glycerol	Melford	Cat# G1345-5L
Glyco-diosgenin (GDN)	Anatrace	Cat# GDN101
HEPES	Thermo Fisher Scientific	Cat# 15630080
HisPur™ Ni-NTA Resin	Thermo Fisher Scientific	Cat# 88221
HRP-conjugated anti-Flag tag	Cell Signaling	Cat# 868615, RRID: AB_2800094
Imidazole	Thermo Fisher Scientific	Cat# 122025000
Isopropyl ß-D-1-thiogalactopyranoside (IPTG)	Thermo Fisher Scientific	Cat# 15529019
Jeffamine ED-2001 pH 7.0	Hampton Research	Cat# HR2-597
Kanamycin	Gibco	Cat# 11815024
Lauryl maltose neopentyl glycol (LMNG)	Anatrace	Cat# NG310
Lysogeny Broth (LB)	Formedium	Cat# LBX0103
$MgCl_2$	New England Biolabs	Cat# B9021S

(*Continued on next page*)

Continued

REAGENT or RESOURCE	SOURCE	IDENTIFIER
$MnCl_2$	Thermo Fisher Scientific	Cat# J63150.AD
NaCl	Sigma Aldrich	Cat# S9888
NEBuilder Hifi DNA assembly Master Mix	New England Biolabs	Cat# E2621L
Nuclease free water	New England Biolabs	Cat# B1500L
PBS (Phosphate-Buffered Saline) Tablets	Thermo Fisher Scientific	Cat# 003002
PEG8000	Sigma Aldrich	Cat# 89510
Lambda DNA	Thermo Fisher Scientific	Cat# SD0011
Phenylmethylsulfonyl fluoride (PMSF)	Thermo Fisher Scientific	Cat# PI36978
Pierce™ 3× DYKDDDDK Peptide	Thermo Fisher Scientific	Cat# A36805
Pierce™ Protease Inhibitor Tablets EDTA-free	Thermo Fisher Scientific	Cat# A32965
Proteinase K	Thermo Fisher Scientific	Cat# AM2542
PVDF membranes	Bio-Rad	Cat# 1620177
Q5 DNA polymerase	New England Biolabs	Cat# M0491L
Quick-Load Purple Low Molecular Wright DNA Ladder	New England Biolabs	Cat# N0557S
RNase A	Thermo Fisher Scientific	Cat# EN0531
Spectinomycin	Melford	Cat# S23000-1.0
Sodium citrate tribasic dihydrate	Sigma Aldrich	Cat# 71402
Sodium dodecyl sulphate (SDS)	Melford	Cat# 28312
SYBR Safe DNA Gel Stain	Thermo Fisher Scientific	Cat# S33102
SYBR Gold Nucleic Acid Gel Stain	Thermo Fisher Scientific	Cat# S11494
SYTOX Orange	Thermo Fisher Scientific	Cat# S11368
TAE 50X	Melford	Cat# T60015-1000.0
Tween-20	Sigma Aldrich	Cat# P1379-25ML
Trans-Blot® SD Semi-Dry Transfer Cell	Bio-Rad	Cat# 1703940
Tris	Thermo Fisher Scientific	Cat# 17926
Critical commercial assays		
DNA Clean & Concentrator Kit	Zymo Research	Cat# D4029
GeneJET Genomic DNA Purification Kit	Thermo Fisher Scientific	Cat# K0722
GeneJET Plasmid Miniprep kit	Thermo Fisher Scientific	Cat# K0503
RNeasy kit	Qiagen	Cat# 74104
Deposited data		
Sequencing reads of phage escape mutants	This study	Figshare: https://doi.org/10.6084/m9.figshare.21652433.v1
Sequencing reads of T2 infecting YFP and Kiwa cells	This study	Figshare: https://doi.org/10.6084/m9.figshare.29025803
RNA seq data of T7s and T7s mutant phage infecting YFP or Kiwa cells	This study	Figshare: https://doi.org/10.6084/m9.figshare.29029154
Atomic coordinates and cryo-EM density map of KwaA tetramer with C2 symmetry	This study	PDB: 9MRG; EMDB: EMD-48556
Atomic coordinates and cryo-EM density map of KwaA tetramer with C4 symmetry	This study	PDB: 9MRR; EMDB: EMD-48562
Atomic coordinates and cryo-EM density map of KwaAB complex	This study	PDB: 9MRX; EMDB: EMD-48564
Atomic coordinates and cryo-EM density map of local KwaAB complex	This study	PDB: 9O01; EMDB: EMD-49973
KwaB dimer-of-dimers crystal structure	This study	PDB: 9MTN
KwaB dimer crystal structure	This study	PDB: 9NYU
Oligonucleotides		
All DNA oligonucleotides are listed in Table S6	IDT	N/A

(*Continued on next page*)

Continued

REAGENT or RESOURCE	SOURCE	IDENTIFIER
Recombinant DNA		
All plasmids are listed and described in Table S7	N/A	N/A
Software and algorithms		
Adobe Illustrator 24.2	Adobe	N/A
Adobe Photoshop 25.11.0	Adobe	N/A
Alphafold 2 run on COSMIC2 server	Jumper et al.[60] and Cianfrocco et al.[61]	https://cosmic2.sdsc.edu:8443/gateway/login!input.action
BBTools	Bushnell et al.[62]	https://github.com/kbaseapps/BBTools
bcl-convert v3.9.3	N/A	https://support.illumina.com/downloads/bcl-convert-v4-0-3-installer.html
Breseq v0.37.0	Deatherage and Barrick[63]	https://github.com/barricklab/breseq/releases
ChimeraX v1.6.1	Meng et al.[64]	https://www.rbvi.ucsf.edu/chimerax/download.html
ClipKIT	Steenwyk et al.[65]	https://github.com/JLSteenwyk/ClipKIT
Clustal Omega	Sievers et al.[66]	https://www.ebi.ac.uk/jdispatcher/msa/clustalo
Coot	Emsley et al.[67]	https://www2.mrc-lmb.cam.ac.uk/ personal/pemsley/coot/
COSMIC[2]	Cianfrocco et al.[61]	https://cosmic-cryoem.org/
cryoSPARC	Punjani et al[68]	https://cryosparc.com/
DALI	Holm and Laakso[69]	https://ekhidna.biocenter.helsinki.fi/dali_server/
DeepTMHMM	Hallgren et al.[70]	https://dtu.biolib.com/DeepTMHMM
GraphPad Prism 10	GraphPad	N/A
Geneious prime 2023.0.1	Geneious	https://www.geneious.com/updates
geNomad v1.7	Camargo et al.[71]	https://github.com/apcamargo/genomad
GPSite	Yuan et al.	https://github.com/biomed-AI/GPSite; https://bio-web1.nscc-gz.cn/app/GPSite
HHpred	Söding et al.[72]	https://toolkit.tuebingen.mpg.de/tools/hhpred
HISAT2	Kim et al.[73]	https://daehwankimlab.github.io/hisat2/
HKL suite	HKL Research	https://www.hkl-xray.com/
IQ-tree2	Mihn et al.[74]	http://www.iqtree.org/
iTOL v6	Letunic and Bork[75]	https://itol.embl.de/
Leginon software	NRAMM	https://emg.nysbc.org/projects/leginon/wiki/Leginon_Homepage
MiniMap2	Li[76]	https://github.com/lh3/minimap2
MM-align	Mukherjee and Zhang[77]	https://zhanggroup.org/MM-align/
MMseqs2	Steinegger and Söding[78]	https://github.com/soedinglab/MMseqs2
ModelFinder	Kalyaanamoorthy et al.[79]	http://www.iqtree.org/ModelFinder/
Muscle5	Edgar[80]	https://www.drive5.com/muscle/
PADLOC version 1.1.0 with database version 1.4.0	Payne et al.[13]	https://github.com/padlocbio/padloc
PHASER	McCoy et al.[81]	https://phenix-online.org/download/documentation/phenix/out-of-date/phenix-1.3b/phaser_doc/phaser-2.0.html
PHENIX	Adams et al.[82]	https://phenix-online.org
NCBI Prokaryotic Genome Annotation Pipeline (PGAP)	Li et al.[83]	https://www.ncbi.nlm.nih.gov/refseq/annotation_prok/
Protter	Omasits et al.[84]	https://wlab.ethz.ch/protter/start/
SerialEM software	(Mastronarde, D. N. 2005)[85]	https://bio3d.colorado.edu/SerialEM/download.html
SPROF-GO	Yuan et al.[27]	https://github.com/biomed-AI/SPROF-GO
TPMCaltulator	Vera Alvarez et al.[86]	https://github.com/ncbi/TPMCalculator

(*Continued on next page*)

Continued

REAGENT or RESOURCE	SOURCE	IDENTIFIER
TreasureIsland	Banerjee et al.[87]	https://github.com/FriedbergLab/GenomicIslandPrediction
UFBoot2	Hoang et al.[88]	http://www.iqtree.org
NIS Elements Software 4.10.04	Nikon	https://www.microscope.healthcare.nikon.com/products/software/nis-elements
Other		
CLARIOstar Plus microplate reader	BMG LABTECH	Cat# CLARIOstar Plus
Nikon A1R confocal microscope	Nikon	https://www.nikon.com/products/microscope-solutions/lineup/confocal/a1/
Invitrogen iBright 1500 imaging system	Thermo Fisher Scientific	Cat# A44114
Nanodrop 2000	Thermo Fisher Scientific	Cat# ND2000
Refeyn TwoMP mass photometer	Refeyn	https://refeyn.com/twomp
Superose™ 6 Increase 10/300 GL column	Cytiva	Cat# 29091596
Superdex™ 200 increase 10/300 GL column	Cytiva	Cat# 28990944
Titan rios G2 transmission electron microscope	FEI	https://www.thermofisher.com/uk/en/home/electron-microscopy/products/transmission-electron-microscopes/krios-cryo-tem.html?SID=srch-srp-KRIOSG4TEM
Vitrobot Mark IV	FEI	https://www.thermofisher.com/us/en/home/electron-microscopy/products/sample-preparation-equipment-em/vitrobot/instruments/vitrobot-mark-iv.html

EXPERIMENTAL MODEL AND STUDY PARTICIPANT DETAILS

Bacterial strains and phages

E. coli Dh5α, BL21-AI, BL21-AIΔRecB, BL21-AIΔRecC, BL21-AIΔRecD,[51] KEIO BW25113 and JW0454[89] were grown at 37 °C in Lysogeny Broth (LB) for liquid cultures or LB agar (LBA, 1.5 % (w/v) agar) for solid cultures. Whenever applicable, LB was supplemented with chloramphenicol (25 μg/mL), spectinomycin (50 μg/mL), Isopropyl ß-D-1-thiogalactopyranoside (IPTG, 1 mM) or L-Arabinose (0.2 %), to ensure maintenance of plasmids or induce protein expression. Phage infection was performed in LB at 37 °C. Phages were propagated by infecting *E. coli* BL21-AI grown to an optical density at 600 nm (OD_{600}) of 0.2-0.4 with 5-10 μL of a phage lysate. Infected cultures were grown for at least 4 hours or until culture collapse. The culture was then centrifuged at 11,000 × *g*, 4 °C for 15 min to remove cell debris, and the supernatant was filter sterilized through a 0.22 μm filter. Phage lambda with a frameshift mutation in Gam[47] was produced in BL21-AI ΔRecB. All strains and phages used in this study are listed in Table S4.

METHOD DETAILS

Plasmid and strain construction

Kiwa systems from *E. coli* ECOR8, ECOR12, ECOR49, and D9 were amplified by Q5 polymerase (New England Biolabs) using primers indicated in Table S5. Kiwa from *Ralstonia mannitolilytica* SN82F48 was ordered synthetically as a gBlock (Integrated DNA Technologies) (Table S5). Kiwa systems under with native promoters were amplified from the respective host strain using primers listed in Table S5, in reactions that added regions of homology for cloning into pUOS016 using NEBuilder Hifi DNA Assembly Mastermix. When appropriate, deletions, mutations and truncations of Kiwa operons were engineered by around-the-horn PCR with primers listed in Table S5. For protein purification, His-tagged KwaB of ECOR8 or ECOR12 Kiwa was constructed by around the horn PCR on pUOS017 or pUOS018 respectively, introducing a 9xHis tag at the N-terminus of KwaB with primers listed in Table S5. Phage proteins gp5.7/T3p30 and gp17/T3p48 were amplified from the genome of T7s or T3 respectively using the primers indicated in Table S5. These proteins were cloned into pCDF1-b (Novagen) under the control of a T7 promoter. Lambda GamL was amplified from Lambda genomic DNA and cloned into pCDF1-b by Gibson assembly. The GamS version was constructed by around the horn PCR. Phage T7 Ocr was cloned into pCOLA (Novagen) by around the horn PCR on pUOS040 using primers listed in Table S5. All plasmids were transformed into *E. coli* Dh5α, extracted using the GeneJET Plasmid Miniprep kit (Thermo Fisher), verified by Sanger sequencing (Eurofins Genomics) and transformed into electrocompetent *E. coli* BL21-AI. Plasmids built for this study are listed in Table S5.

Plaque assays

Phages were ten-fold serially diluted in LB and spotted on soft agar plates (0.7 % (w/v) agar) of *E. coli* BL21-AI containing a control plasmid or individual Kiwa systems. For spot assays in strains expressing phage proteins *in trans*, induction was performed with 0.2% or 0.02% L-arabinose. Plates were left to dry at room temperature and incubated overnight at 37 °C. Plaque forming units (PFUs) were determined by counting the plaques after overnight incubation. Whenever plaques were too small to be counted, a clear lysis area was set to be equal to 1 PFU or indicated by an open dot on the bar graph. Fold defence was determined by calculating the ratio of phage concentration of Kiwa expressing strain relative to control strains.

Time post infection assays

Overnight bacterial cultures of *E. coli* BL21-AI with a control plasmid or individual Kiwa systems were diluted 1:100 in LB medium and grown at 37 °C with agitation until an OD_{600} of ≈0.3. Cultures were normalized and infected with phage T4 at an MOI of 3. A sample was taken at different time points post infection, serially diluted, and total phages were quantified by plaque assay on a phage-sensitive bacterial lawn (*E. coli* BL21-AI + pUOS016). For colony forming units, samples were washed twice with PBS 1x, serially diluted and spotted onto LBA plates. PFUs and CFUs were counted after overnight incubation at 37 °C.

Conjugation assays

S17 cells containing plasmid pSEVA637 (donor) and BL21-AI cells containing the Kiwa systems or control plasmid (recipient) were grown overnight with antibiotics (gentamycin and chloramphenicol, respectively). Recipient cells were diluted 1:2 in LB and grown for at least 3h, while donor cells were diluted 1:100 in LB and grown until an OD_{600} of 0.3 at 37 °C, 180 rpm. 750 µl of donor cells were mixed with 250 µl of recipient cells, centrifuged at 9000 × *g* for 5 min, and resuspended in 25 µl of LB. The cell mixture was spotted onto LBA plates and incubated overnight at 30 °C. The cells were recovered from the plates and resuspended in 1 ml of PBS 1x. Two or ten-fold dilutions of this cell suspension were spotted onto LBA plates supplemented with chloramphenicol (for total recipient cell count) and LBA plates supplemented with chloramphenicol and gentamycin (for conjugant cell count). The plates were incubated at 37 °C for 18-24h and cells counted. Conjugation efficiency was calculated as the ratio (%) of conjugants per total recipient cells.

DNA replication assay

Overnight bacterial cultures of *E. coli* BL21-AI with a control plasmid or individual Kiwa systems were diluted 1:100 in LB medium and grown at 37 °C with agitation until cultures reached an OD_{600} of ≈0.3. Cultures were normalized and infected with phage T2 at an MOI of 3. At 0 and 15 minutes post infection, a 5 ml sample was taken and centrifuged (15,000 × *g*, 5 min, 4 °C). The cell pellets were snap frozen using liquid nitrogen and stored at -80 °C. Total DNA was extracted using the GeneJET Genomic DNA Isolation kit (Thermo Fisher), using the Gram-negative protocol. Samples were sequenced at SeqCenter (Pittsburgh, PA, USA), where sample libraries were prepared using the Illumina DNA Prep kit and IDT 10bp UDI indices, and sequenced on an Illumina NextSeq 2000, producing 2×151bp reads. Demultiplexing, quality control and adapter trimming was performed with bcl-convert (v3.9.3). Reads were aligned to *E. coli* BL21-AI and phage T2 reference genomes (CP047231 and NC_054931.1) using MiniMap2[76] in Geneious prime 2023.0.1. Phage replication was determined by calculating the average read depth of the phage genome in infected samples and normalising it to the average read depth of the host genome in uninfected samples. This approach corrects for phage-induced host DNA degradation and enables comparison of phage DNA levels between Kiwa-expressing and control cells. The percentage reduction in replication efficiency of phage in Kiwa-expressing cells was calculated as the relative change in normalised phage DNA abundance to control cells.

Bacterial two-hybrid assay

Expression plasmids were cloned by fusing the T18 or T25 fragments of adenylate cyclase (CyaA) of *Bordetella pertussis* to either end of KwaB or the Lambda Gam protein, using primers listed in Table S5. *E. coli* BTH101 cells (F-, *cya-99*, *araD139*, *galE15*, *galK16*, *rpsL1* (*Str r*), *hsdR2*, *mcrA1*, *mcrB1*) were co-transformed with pairs of T18 and T25 plasmids, or control plasmids containing the leucine zipper motif of GCN4. Co-transformants were grown in LB supplemented with IPTG (0.5 mM), Ampicillin (100 µg/mL) and Kanamycin (50 µg/mL) at 30 °C with agitation. Overnight cultures were then spotted on LB agar plates supplemented with IPTG (0.5 mM), 5- bromo-4-chloro-3-indolyl-β-D-galactopyranoside (X-Gal, 40 µg/mL) and antibiotics. Plates were incubated at 30°C up to 48 hours before imaging.

RecBCD mutant assays

Strains with individual deleted RecBCD subunits were transformed by electroporation with a control or Kiwa plasmids and recovered on LBA supplemented with kanamycin (50 µg/mL), chloramphenicol (25 µg/mL) and spectinomycin (50 µg/mL). Colonies were picked and grown overnight at 37 °C. Spot assays were performed with phages T4, T4Δgp2, $Lambda_{vir}$, and $Lambda_{vir}$ with a frameshift mutation in Gam.

Isolation and sequencing of escape phages

Escape phages were isolated by picking single plaques at the lowest dilution of a spot assay on a lawn of *E. coli* cells expression Kiwa. The resistant phenotype of each escape phage was determined by comparing the EOP of the escape phage to the EOP of

the wild type phage in the presence of Kiwa. Isolated phages were further propagated by infecting a liquid culture of Kiwa as described above. Phage lysates were pelleted following the NaCl/PEG8000 precipitation protocol as previously described.[90] The phage pellets were re-suspended in LB, and treated with DNase I and RNase A (1 μg/mL each) for 30 min at room temperature. EDTA (20 mM), proteinase K (50 μg/mL) and SDS (0.5%) were added to the suspension and incubated overnight at 56 °C. DNA was extracted using the Zymo Clean & Concentrator kit (Zymo Research). Samples were sequenced at SeqCenter, where sample libraries were prepared using the Illumina DNA Prep kit and IDT 10bp UDI indices, and sequenced on an Illumina NextSeq 2000, producing 2×151bp reads. Demultiplexing, quality control and adapter trimming was performed with bcl-convert (v3.9.3). Mutations were identified by mapping sequencing reads to the respective reference phage genomes (NC_003298 for T3 and Table S4 for T7s) using Breseq[63] v0.37.0 with default parameters. Only mutations that occurred in the isolated mutant but not in the wild type phage were considered. Silent mutations within protein-coding regions were also neglected.

Amplification of mutant phages in cells expressing wild type tail fibres

Escape mutant T3 phages were propagated in cells expressing wild type T3p48 in *trans* for 4h at 37 °C, 180 rpm. The cultures were centrifuged at 9,000 × *g*, the supernatant recovered, filtered (0.2 μm PES), and stored at 4 °C until further use. The recovered phages were ten-fold diluted and spotted onto double layer agar with control or Kiwa-expressing cells, or onto double layer agar with Kiwa-expressing control or ΔwaaJ cells. The plates were incubated overnight at 37 °C for determining phage titres.

Protein expression and purification

Overnight cultures of *E. coli* BL21-AI with N-terminal 9xHis KwaB from ECOR8 or ECOR12 were diluted in LB supplemented with antibiotics, and grown at 37 °C with agitation until an OD_{600} of ≈0.6. Grown cultures were incubated on ice for 1 hour and protein expression was induced with L-arabinose (0.2 %) and IPTG (1 mM), followed by overnight incubation at 20 °C and 150 rpm. The overnight cultures were harvested by centrifugation (8,000 × g, 30 min, 4 °C). The supernatant was discarded and the cell pellets were re-suspended in lysis/wash buffer (50 mL per 1 L of initial culture, 100 mM Tris-HCl, 500 mM NaCl, 1 mM DTT, 5% glycerol, 40 mM imidazole, pH 8.0) supplemented with Pierce™ Protease Inhibitor Tablets EDTA-free (Thermo Fisher). Cell lysis was performed three times in a cooled French press (15Gpa). The cell lysate was centrifuged (17,000 × g, 30 min, 4 °C) and debris were removed by filtration (0.45 μm PES). The filtered supernatant was incubated with HisPur™ Ni-NTA Resin (Thermo Fisher) (500 μL/50 mL lysate) pre-washed with 20 mL of lysis/wash buffer for 30 min at 4 °C. The sample was loaded onto a 5 mL Pierce™ Disposable Column (Thermo Fisher) for gravity-flow affinity chromatography. The column was washed with 15 mL of ice-cold lysis/wash buffer, and the protein was eluted with ice-cold elution buffer (100 mM Tris-HCl, 500 mM NaCl, 1 mM DTT, 5% glycerol, 250 mM imidazole, pH 8.0). Pooled fractions were concentrated (Amicon Centrifugal concentrator with Ultracel membrane, 10 kDa MWCO), and the buffer exchanged to running buffer (100 mM Tris-HCl, 150 mM NaCl, 1 mM DTT, 5% glycerol, pH 8.0). The resulting protein sample was subjected to size exclusion chromatography using a Superdex 200 increase 10/300 GL (Cytiva) column equilibrated with running buffer with 0.5 mL/min flow rate using running buffer as a mobile phase. Fractions of interest were analysed by SDS-PAGE, snap frozen in liquid nitrogen and stored at -80 °C until further use.

KwaA expression and purification

The genes encoding KwaA (UniProt: P0DW45) and KwaB (UniProt: P0DW46) from *Escherichia coli* O55 were codon-optimized and synthesized by IDT. They were then individually cloned into the pET21a vector (Novagen) with ampicillin resistance and the pYB100 vector (NovoPro) with kanamycin resistance. KwaA was fused to a C-terminal Flag tag, while KwaB was fused to a C-terminal His6 tag.

The O55 KwaA membrane protein was overexpressed in C43 cells, a derivative of *Escherichia coli* BL21(DE3), and induction was carried out using 0.5 mM IPTG (GoldBio) at 16 °C for 20 hours. The cells were harvested by centrifugation and resuspended in a lysis buffer (25 mM Tris, pH 8.0, 500 mM NaCl, 2 mM β-mercaptoethanol, and cOmplete (EDTA-free protease inhibitor). Cell lysis was achieved through sonication, after which 1% (w/v) Lauryl Maltose Neopentyl Glycol (LMNG, Anatrace) and 0.1% (w/v) cholesteryl hemisuccinate (CHS, Anatrace) were added to solubilize the proteins at 4 °C for 3 hours. Insoluble material was cleared by centrifuging at 22,000 rpm for 1 hour using a JA-20 fixed-angle rotor (Avanti J-E series centrifuge, Beckman Coulter). The resulting supernatant was incubated with anti-FLAG M2 affinity gel (Sigma, A2220) while rotating at 4 °C for another 3 hours. The sample was subsequently loaded onto a gravity column and thoroughly washed with Wash Buffer I (25 mM Tris, pH 8.0, 500 mM NaCl, 2 mM β-mercaptoethanol, 0.1% (w/v) LMNG, and 0.01% (w/v) CHS), followed by Wash Buffer II (25 mM Tris, pH 8.0, 500 mM NaCl, 2 mM β-mercaptoethanol, 0.001% (w/v) LMNG, 0.0001% (w/v) CHS, and 0.00033% Glyco-diosgenin (GDN, Anatrace)). The protein was then eluted with Wash Buffer II containing 0.2 mg/ml 3× DYKDDDDK Peptide (Pierce) while rotating for 30 minutes at 4 °C. The elution was then concentrated and further purified using size exclusion chromatography (SEC) on a Superdex 200 Increase 10/300 GL column (GE Healthcare) equilibrated with SEC buffer (25 mM Tris, pH 8.0, 500 mM NaCl, 2 mM β-mercaptoethanol, 0.001% (w/v) LMNG, 0.0001% (w/v) CHS, and 0.00033% GDN). Fractions eluted at around 15 ml, indicating tetrameric assembly, were collected, concentrated, and prepared for SDS-PAGE and cryo-EM analysis.

KwaB expression and purification

KwaB protein purification for crystallization began with its expression in BL21 (DE3) cells, using a C-terminal His tag. Protein expression was induced with 0.5 mM IPTG, and the culture was grown at 16 °C with shaking at 220 rpm for about 20 hours. The cells were then harvested by centrifugation at 4,000 rpm for 15 minutes, and the pellet was resuspended in a lysis buffer containing 25 mM Tris (pH 8.0), 500 mM NaCl, 5% glycerol, 2 mM β-mercaptoethanol, and PMSF. After cell disruption using sonication, the lysate was centrifuged at 22,000 rpm for 1 hour to separate the soluble fraction. The clarified lysate was then applied to a Ni-NTA gravity column, where the protein underwent flow-through, washing, and elution steps. The eluted protein solution contained 25 mM Tris (pH 8.0), 150 mM NaCl, 5% glycerol, 2 mM β-mercaptoethanol, and 500 mM imidazole. To further purify the sample and remove any nucleic acid contaminants, it was passed through a heparin column. Finally, the protein underwent gel filtration using a Superdex 200 Increase column to exchange it into the crystallization buffer, which contained 25 mM HEPES (pH 7.5), 150 mM NaCl, 5% glycerol, and 2 mM DTT.

KwaAB expression and purification

For cryo-EM analysis of the KwaA and KwaB complex, KwaA-flag and KwaB-His6 were co-expressed and purified using anti-FLAG resin, following the same protocol as that used for isolating KwaA alone. The fraction peaks from the Superose 6 Increase column revealed the high molecular weight KwaAB complex at 11.8 ml and the low molecular weight KwaAB complex at 14.5 ml, as indicated by the SDS-PAGE results. Additionally, the MscK protein co-eluted with the high molecular weight complex, which was also confirmed by SDS-PAGE analysis.

Cryo-EM sample preparation and data collection

For membrane bound KwaA, the purified protein was concentrated to 4 mg/ml using a Superose 6 Increase column. A 4 μl aliquot of the sample was applied to glow-discharged holey gold grids (UltrAuFoil 300 mesh R1.2/1.3). The grids were blotted for 3 seconds with a force setting of 0 at 6 °C and 100% humidity, then rapidly frozen in liquid ethane using a Vitrobot Mark IV (FEI). Data collection was performed at the Memorial Sloan Kettering Cancer Center (MSKCC) using a Titan Krios G2 transmission electron microscope (FEI) operating at 300 kV and equipped with a K3 direct detector, controlled by SerialEM software. Movies were recorded in super-resolution mode with a total electron dose of 53 $e^-/Å^2$, a defocus range of -0.8 to -2.2 μm, and a pixel size of 1.064 Å. The cryo-EM sample preparation for the KwaAB complex was performed similarly to that of KwaA alone. The peak corresponding to the high molecular weight complex from the Superose 6 Increase column was collected and concentrated to 4.5 mg/ml for cryo-EM analysis. Data collection was carried out using a Titan G2 transmission electron microscope (FEI) operating at 300 kV, equipped with a K3 electron detector, and controlled by Leginon software at the New York Structural Biology Center (NYSBC). The defocus range was set between -0.8 to -2.2 μm, with a pixel size of 0.826 Å and a total electron dose of 58.73 $e^-/Å^2$ in super-resolution mode.

Cryo-EM data processing

For KwaA structure determination, a total of 6,054 movies was processed using cryoSPARC,[68] Patch motion correction and patch contrast transfer function (CTF) estimation were applied to correct for drift and estimate CTF parameters, respectively. Micrographs with ice contamination, high astigmatism, or poor CTF fit resolution were excluded by setting appropriate threshold ranges using the 'Manually Curate Exposures' job. High-quality micrographs were processed using the Blob picker and extract jobs, followed by 2D classification to generate templates for the template picker. Before 2D classification, the "Remove duplicate particles" job was applied to eliminate overlapping or duplicate particles. Three rounds of 2D classification were then performed to discard junk particles, resulting in a selection of 1,849,825 high-quality particles for subsequent 3D modelling. Two rounds of ab initio reconstruction, with class similarity adjustments, and heterogeneous refinement revealed two distinct volumes with C2 and C4 symmetries. These volumes were further refined using homogeneous and non-uniform refinement. The C2 symmetry reconstruction utilised 312,352 particles, achieving a resolution of 3.69 Å, which enabled precise model building. The C4 symmetry reconstruction, based on 278,569 particles, reached a resolution of 4.28 Å, sufficient for main-chain fitting.

To determine the structure of the KwaAB complex, 5,475 micrographs were collected using the K3 camera, and the movies were processed using the same procedure. Following particle selection through Blob picking and template-based methods, 1,731,427 particles were chosen for 2D classification. From these 2D images, the KwaA-KwaB complex and Msck protein were separated, resulting in 182,763 particles for the KwaAB complex and 90,497 particles for the MscK protein. The particles from the KwaA-KwaB complex were subjected to ab-initio reconstruction to generate initial models, followed by heterogeneous refinement to enhance the density map's quality. The best class from the heterogeneous refinement was selected and further polished using homogeneous and non-uniform refinement, achieving a 3.75 Å resolution structure with C4 symmetry. This level of detail allowed for accurate model building of the KwaA tetramer bound to KwaB dimers. To improve the density quality at the interfaces between KwaA-KwaB and between KwaB dimers, 73,572 particles were subjected to symmetry expansion using C4 symmetry, generating a dataset of 294,296 particles for local refinement. This dataset was then refined without symmetry by applying a mask, created using Relion's "Mask creation" tool, focused on the KwaA monomer and KwaB dimer. The final local refinement yielded a 3.86 Å resolution map, in which the side-chain densities are clearly resolved, particularly at the KwaA-KwaB and KwaB dimer interfaces, allowing detailed

analysis of specific interactions. For the MscK protein group, the same protocol as the KwaAB complex was followed, achieving a resolution of 4.14 Å, which enabled fitting the MscK heptamer in its closed state. All the resolution estimations were based on a Fourier shell correction of 0.143 cutoff.

Crystallisation and data collection

KwaB crystals were obtained at 20 °C using the hanging-drop vapor diffusion technique. For this, 1 μL of protein solution was mixed with 1 μL of reservoir solution containing either 0.1 M Tris (pH 8.5) and 5% (w/v) PEG8000 for the KwaB dimer-of-dimer crystals or 0.1 M sodium citrate tribasic dihydrate (pH 5.0) and 30% (v/v) Jeffamine® ED-2001 (pH 7.0) for the KwaB dimer crystals. Crystals formed under both conditions were cryoprotected by adding 25% glycerol to the reservoir solution before being flash-cooled in liquid nitrogen. Diffraction data were collected at the FMX beamline of NSLS-II at Brookhaven National Laboratory and processed using the HKL suite (HKL Research).

Model building, structure refinement, and visualisation

The KwaA tetramer and KwaB dimer models were predicted using Alphafold2,[60] while the MscK model was based on the published heptamer structure (PDB: 7UW5).[19] The KwaAB model was constructed by fitting the KwaA tetramer and KwaB dimer separately, followed by structure building in Coot (Crystallographic Object-Oriented Toolkit).[67] For the KwaB dimer of dimers crystals, the structure was solved by molecular replacement using PHASER[81] with the AF3-predicted KwaB dimer model (iPTM: 0.74, pTM: 0.75). A 'simple one-component interface' was used to identify two copies of the input model. For the KwaB dimer crystals, the same AF3-predicted dimer model was used, but only a single copy was searched. All atomic coordinates were refined against the map in PHENIX.[82] Figures were prepared using UCSF Chimera[91] and USCF ChimeraX[92] with the final image layout created in Adobe Photoshop and Illustrator.

Modelling the KwaAB supercomplex

The KwaAB supercomplex model was constructed from a low-resolution cryo-EM density map, which revealed three repeating KwaAB basic units. Each basic unit comprises a KwaA tetramer and four KwaB dimers ($KwaA_4B_8$). To build the supercomplex, we first aligned the KwaA monomer from the high-resolution basic unit to the smaller local model consisting of one KwaA monomer and one KwaB dimer ($KwaA_1B_2$; RMSD: 0.698 Å). This initial alignment provided a reference scaffold for accurately positioning the second $KwaA_4B_8$ unit by aligning its KwaB dimer (RMSD: 0.855 Å). Subsequent KwaAB units (third to fifth) were sequentially added by aligning their KwaB dimers to the previously positioned unit. The final five-unit supercomplex model fits well with the observed low-resolution cryo-EM density, which initially revealed only three basic units.

AlphaFold prediction and visualisation

To predict the structure of the KwaB-Gam complex, we used AlphaFold2[60] via the ColabFold[93] implementation. Amino acid sequences of two full-length KwaB molecules and two full-length GamS molecules were provided as input, and five structural models were generated. These models were ranked based on AlphaFold confidence metrics, including pLDDT scores and predicted aligned error (PAE) heatmaps. The model with the highest overall confidence was selected for further analysis.

For the KwaB-16mer dsDNA, KwaB-12nt ssDNA, and KwaA-KwaB-dsDNA complexes, we used AlphaFold3.[94] For the KwaB-16mer dsDNA complex, we modelled two full-length KwaB molecules with one 16-mer dsDNA strands (sequence: GTCAGACATGATTGCC and its complement). For the ssDNA complex, we modelled two full-length KwaB molecules with one 12-nt ssDNA strands (sequence: GACATGATTGCC). The KwaA-KwaB-dsDNA complex was modelled with four full-length KwaA molecules, eight full-length KwaB molecules, and four 16-mer dsDNA strands (sequence: GTCAGACATGATTGCC and its complement).

Following structure prediction, visualisation and analysis were performed using a Jupyter Notebook available at colab.research.google.com/github/Ash100/Biopython/AF3_Results_Visualization.ipynb. This tool was used to generate PAE heatmaps to assess confidence in predicted intermolecular contacts. pLDDT scores was further analysed by saving B-factor attributes in ChimeraX and averaging atomic values per residue. Final pLDDT plots were generate in Excel for visual comparison across models.

KwaB mutants' expression and purification

KwaB mutants targeting the DNA-binding site were designed based on the AF3 model. Two mutants, named KwaB 3-mut (R142A/R167A/K187A) and KwaB 6-mut (R142A/R167A/K187A/R233A/N134A/D169A), were constructed as follows: the genes were codon-optimized and synthesized using IDT gBlock fragments, then cloned into the pYB100 vector using the Gibson cloning kit. Expression and purification of the mutants followed the protocol described above for crystallisation of the KwaB wild type protein.

Mass photometry

Mass photometry experiments were performed using a Refeyn TwoMP instrument. A pre-assembled 6-well sample cassette (Refeyn) was placed at the centre of a clean sample carrier slide (Refeyn), with each well designated for an individual measurement. To establish the focal point, 15 μL of freshly prepared SEC buffer (25 mM HEPES-NaOH, pH 7.5; 150 mM NaCl; 5% glycerol; and 2 mM DTT) were added to the well. The focus was determined and maintained throughout the measurement using an autofocus system based on

total internal reflection. Purified KwaB protein, prepared in the same SEC buffer, was initially diluted to 500 nM (dimer), and 1 μL of the diluted sample was added to the buffer drop, achieving a final protein concentration of 33.3 nM. Once the autofocus stabilised, movies were recorded for 60 seconds. Data were collected using Refeyn AcquireMP (version 2024.1.1.0) and analysed with Refeyn DiscoverMP (version 2024.1.0.0). Contrast-to-mass calibration was carried out using a BSA protein standard (Sigma), which contained BSA monomers and dimers with molecular masses of 66.5 and 132 kDa, respectively. Statistical analysis was conducted using DiscoverMP, where Gaussian fitting was applied to distribution peaks to determine the average molecular mass of each component.

Electrophoretic mobility shift assay

For the O55 KwaB binding assays with ssDNA or dsDNA, we utilized a 72 nt sequence (5'TGGTTTTTATATGTTTTGTTATGTATTGTTTATTTTCCCTTTAATTTTAGGATATGAAAACAAGAATTTATC) as well as its complementary DNA substrates. The DNA substrates were assembled through self-annealing in an annealing buffer containing 25 mM HEPES (pH 7.5), 150 mM NaCl, and 2 mM $MgCl_2$. For the assembly of DNA with KwaB and mutant KwaB proteins, 10 nM DNA substrates were incorporated into a total volume of 20 μl. Prior to use, ssDNA was denatured by heating the sample at 95°C for 5 minutes, followed by rapid cooling on ice, to minimise secondary structure formation. The ratios of KwaB protein (concentration calculated as dimer) to dsDNA were set at 0, 1, 8, 16, 32, 64, and 128:1, while for ssDNA, the ratios were 0, 1, 4, 8, 16, 32, and 64:1. The protein and DNA substrates were diluted in an annealing buffer that contained an additional 5% glycerol for gel loading. After incubating the mixtures on ice for 1 hour, 10 μl of each was loaded onto a 6% DNA Retardation Gel (Invitrogen) and electrophoresed at 100 V for 35 minutes at 4 °C in 0.5 x TBE buffer. Nucleic acids were visualized using SYBR Gold nucleic acid gel stain (Invitrogen), incubated in the dark for 30 minutes, and imaged using a ChemiDoc imaging system.

Additionally, pUC19 plasmid DNA, *E. coli* BL21-AI gDNA, and phage Lambda gDNA (Thermo Fisher) were used as DNA probes for EMSA assays. 50 ng of dsDNA probe or 150 ng ssDNA (FN0850) were mixed with purified KwaB at 350 nM (concentration calculated as dimer) in assembly buffer 1 (100 mM Tris-HCl, 150 mM NaCl, 1 mM DTT, 5% glycerol, 10 mM $MgCl_2$, pH 8.0) and incubated at 37 °C for 30 minutes. Samples were mixed with blue DNA loading dye and loaded on a 1% agarose gel for electrophoresis. Gels were run at 100 V for 50 minutes in 1X TAE buffer. Nucleic acids were visualised with SYBRSafe or SYBRGold staining and captured with an Invitrogen iBright 1500 apparatus (Thermo Fisher).

To assess the impact of mutations in residues involved in the KwaB-DNA binding surface, purified KwaB wild type (wt) protein and mutants (3-mut and 6-mut) were concentrated to 28 μM (calculated as dimer). A 128:1 ratio of KwaB proteins to DNA substrate was used, with 50 ng of 72-nt single-stranded DNA (ssDNA) or 72-bp double-stranded DNA (dsDNA) added to a total reaction volume of 10 μl. The mixtures were incubated at room temperature for 30 minutes. Subsequently, 3 μl of each sample was loaded onto a 6% DNA retardation gel (12-well), along with 0.2 μl of Quick-Load Purple Low Molecular Weight DNA Ladder (NEB, N0557S). The gel was run at 100 V for 80 minutes at 4°C in 0.5× TBE running buffer. SYBR Gold was used to stain the gel in the dark with gentle shaking for 30 minutes, followed by three washes with ddH2O. The gel was imaged using a ChemiDoc imaging system.

In vitro nuclease activity

Purified PCR amplicons, pUC19 plasmid DNA, *E. coli* BL21-AI gDNA, phage Lambda gDNA (Thermo Fisher) and oligos were used as substrates for cleavage assays. Target cleavage assays were performed in a 10 μl reaction mixture containing 50 ng dsDNA or 600 ng ssDNA (FN0850) substrate and 1.14 μM protein (calculated as dimer) in cleavage buffer (100 mM Tris-HCl, 150 mM NaCl, 1 mM DTT, 5% glycerol, pH 8.0) supplemented with ddH_20, $MgCl_2$ (10 mM) or $MnCl_2$ (10 mM), and ATP (1 mM). Assays were allowed to proceed at 37 °C for 2 hours and stopped by addition of proteinase K (Thermo Fisher) and incubated at 55 °C for 15 minutes. Samples were mixed with purple DNA loading dye (with EDTA) (NEB) and loaded on a 1% or 1.5% (oligos only) agarose gel for electrophoresis. Gels were run at 100 V for 50 minutes in 1x TAE buffer. Nucleic acids were visualised with SYBRSafe or SYBRGold (oligos only) staining and captured with an Invitrogen iBright 1500 apparatus (Thermo Fisher).

Fluorescence anisotropy binding assays

To determine DNA binding affinities of KwaB, serial two-fold dilutions of ECOR8 KwaB (concentration calculated as monomer) were incubated with 0.8 nM FAM-labelled 20-nt ssDNA (top oligo, Table S5) or 20-bp dsDNA (top and bottom oligo, Table S5) for 3 hours at 37 °C in binding buffer (150 mM NaCl, 25 mM HEPES pH 7.5, 0.05 Tween-20). Data were recorded at 37 °C in a CLARIOstar Plus multi-detection plate reader (BMG Labtech) equipped with a fluorescence polarization optical module (λ_{ex} = 485 nm; λ_{em} = 520 nm). Data were fit in GraphPad Prism 10 using a one-step binding model, and extrapolated start and end points were used to normalize the calculation of fraction bound. For Gam competition binding experiments, 1 μM KwaB (calculated as monomer) was preincubated with 50 nM ss/dsDNA as described above, and then further supplemented with a final concentration of 10 μM GamS (New England Biolabs), and then measurements were performed as described above.

Pull-down assay for GamS and KwaB

The full-length GamS was fused to a C-terminal Flag tag and cloned into the pET21a vector. It was then co-transfected into *E. coli* with the KwaB-His plasmid at a 4:1 molar ratio, followed by selection based on ampicillin and kanamycin resistance. The selected colonies were then transferred to 1 L of LB liquid medium, induced, and harvested using the same method. The bacteria were lysed

with Lysis buffer (25 mM Tris, pH 8.0, 300 mM NaCl, 5% glycerol, 2 mM DTT), followed by low-temperature sonication and centrifugation to obtain the supernatant. This supernatant was incubated with Flag beads for 3 hours, after which the beads were washed, and the target protein was eluted using 3x Flag peptide. The eluate was concentrated and loaded onto Superose 6 Increase column, and peaks 2 and 3 were collected for gel analysis. SDS-PAGE results demonstrated the co-elution of KwaB and Gam.

As controls, KwaB-His and GamS-Flag were individually expressed and purified following the same protocol describe above. For SEC, each protein was concentrated and injected separately onto the same Superose 6 Increase column, using identical injection volumes and the same AKTA system as employed for the co-purified proteins.

Western blot

To verify the expression of mutant KwaAB proteins, we performed western blot analysis using Flag-tagged KwaA and His-tagged KwaB. Briefly, ECOR49-derived KwaA and its mutants were overexpressed in *E. coli* C43 cells, while ECOR49- and O55:H7-derived KwaB were overexpressed in *E. coli* BL21 cells. Cultures (500 mL) in TB medium were induced with 0.5 mM IPTG at 16 °C for 20 hours. Cells were harvested by centrifugation and resuspended in 20 mL of lysis buffer containing 25 mM Tris-HCl (pH 8.0), 300 mM NaCl, 2 mM β-mercaptoethanol, and cOmplete EDTA-free protease inhibitors. Cell lysis was carried out by sonication at 45% maximum power (3 s on, 5 s off) for 10 minutes at 4 °C. KwaB lysates were clarified by centrifugation at 22,000 rpm for 1 hour. For KwaA, 1% (w/v) LMNG and 0.1% (w/v) CHS were added to the lysate, which was rotated at 4 °C for 3 hours to solubilize membrane proteins before centrifugation. The resulting supernatants were loaded onto SDS-PAGE gels after adjusting concentrations based on the internal reference protein GroEL.

Proteins were transferred to PVDF membranes using a semi-dry transfer system (Bio-Rad) at a constant 15 V for 20 minutes. Membranes were then blocked with 5% (w/v) non-fat dry milk (Bio-Rad) in 0.05% Tween-20/TBS buffer for 1 hour at room temperature. Primary detection was performed using HRP-conjugated anti-Flag tag (86861S, Cell Signaling) or anti-6His tag (YK382778, Invitrogen) antibodies at a 1:1000 dilution for 1 hour at room temperature. For GroEL detection (NB018822, Fisher Scientific), the antibody was diluted 1:3000 and incubated for 1 hour at room temperature. Membranes were washed five times for 5 minutes each in 0.05% Tween-20/TBS. The GroEL membrane was subsequently incubated with goat anti-mouse IgG (AP124P, MilliporeSigma) at a 1:5000 dilution for 45 minutes at room temperature, followed by another five washes. Bound antibodies were visualized using enhanced chemiluminescence reagents (Thermo Scientific) and quantified by densitometry with a ChemiDoc MP imaging system (Bio-Rad).

Confocal microscopy

Overnight cultures of control (YFP) or Kiwa-expressing cells were sub-cultured in LB with antibiotics for 2 hours. Agarose pads were prepared with 1% agarose in LB. Two μl of bacterial culture were seeded onto the agarose pads and covered with microscope cover slips prior to imaging. Confocal images and movies were acquired using a dual point-scanning Nikon A1R-si microscope equipped with a PInano Piezo stage (MCL), using a 60x PlanApo VC oil objective NA 1.40. Movies and images were acquired in galvanometer scanning mode using 488nm Laser (Coherent, 50mW), and a 561 nm Laser (Coherent, 50mW). Image processing and quantification was performed using FiJi software. The phage filtrates were treated with DNase I (1 μg/ml each) for an hour at room temperature. SYTOX orange was added to a final concentration of 2.5 μM, and incubated overnight at 4 °C. Excess dye was removed by centrifuging the stained lysate on a 100 kDa Amicon Ultra (UFC5100) filter and rinsing the dye away with fresh LB four times. The concentrated stained phages were resuspended in 1 ml of fresh LB and stored at 4 °C.

RNAseq

Overnight cultures were diluted with fresh LB supplemented with antibiotics at 1:100 and incubated at 37 °C, 180 rpm for 2 hours. Phages were added to the cells at MOI 10. The cells were harvested by centrifugation after 15 minutes of incubation, and the RNA immediately extracted with RNeasy Kit (Qiagen). Library construction, rRNA depletion, and paired-end Illumina sequencing (Novaseq 6,000, 2 × 150 bp configuration) were performed by Novogene. Genomes of *E. coli* BL-21-AI and T2 phage used in this study were annotated using the PGAP pipeline.[83] The quality of RNA-seq data was assessed using FastQC, and low-quality tiles were removed using BBTools.[62] Reads were mapped to the genome using HISAT2,[73] and the ones corresponding to tRNA and rRNA were discarded. TPM values were calculated using TPMCalculator,[86] and for mathematical purposes, phage genes and bacterial genes were treated as separate datasets.

Bioinformatic analysis

Information on defence systems in 223,143 prokaryotic genomes was retrieved from the PADLOC database.[13,14] Only complete Kiwa systems that contained both KwaA and KwaB gene within the operon, were considered for further analysis (Table S6). For phylogenetic analyses, split KwaB proteins were concatenated into a single sequence, and KwaA and KwaB proteins were dereplicated using MMseqs2 at 90% sequence identity threshold.[78] Contigs encoding representative KwaA and KwaB proteins shorter than 150 and 200 amino acids, respectively, were re-examined. Partial sequences located at the ends of contigs were discarded, and any sequences with updated annotations in the latest RefSeq release (v227) were replaced with the new annotations. The retained sequences (Table S7) were aligned using Muscle5,[80] and sites with more than 99% of gaps were trimmed using ClipKIT.[65] Phylogenetic trees were reconstructed using IQ-Tree2,[74] and the optimal model was picked using ModelFinder from the set of WAG, LG, Q.Pfam, and NQ.Pfam.[79] Support values were estimated using 1,000 ultrafast bootstrap replicates with a hill-climbing nearest neighbour

interchange optimization (UFBoot2),[88] and trees were visualized using iTOL v6.[75] Contigs encoding KwaA and KwaB from the dereplicated set were searched for plasmids and prophages using geNomad v1.7,[71] and genomic islands were identified using TreasureIsland with probability cutoff at 0.95.[87] Additionally, 10 genes upstream and downstream of KwaA and KwaB were annotated using COG profiles.[15] Kiwa genes that are colocalized with at least 2 hallmark genes from MGEs (X category) were labelled as associated with 'other mobilome' (Tables S7).

Protein domains of KwaA and KwaB were identified using HHpred.[72] Transmembrane domains were identified using DeepTMHMM.[70] KwaA proteins with more or less than four transmembrane domains were manually checked for misannotation of the start codon. Sequence alignments of KwaA C-terminus and KwaB were constructed using Clustal Omega[66] and visualised using Geneious Prime v2023.0.1. For KwaB mutants, a total of nine homologs present in the KwaB ECOR8 and ECOR12 cluster were selected and aligned to determine amino acid conservation. KwaA schematic was visualised and adapted from Protter.[84] All structural models were built using Alphafold[60] (AF2) software run on the external COSMIC server[61] using either the multimer or monomer model with complete database settings. Structural similarity was estimated using DALI[69] for monomers, and MM-align[77] for multimers. Structures were visualised using ChimeraX v1.6.1.[64] KwaB functionality was predicted using the Biomedical AI Platform webtool SPROF-GO.[27]

QUANTIFICATION AND STATISTICAL ANALYSIS

Unless stated otherwise, experiments were performed in biological triplicates and are represented as the mean and standard deviation. Statistical significance was calculated by ratio paired t-test or by two-way ANOVA with sidak's multiple comparison test, with a significance level of 0.05.

Supplemental figures

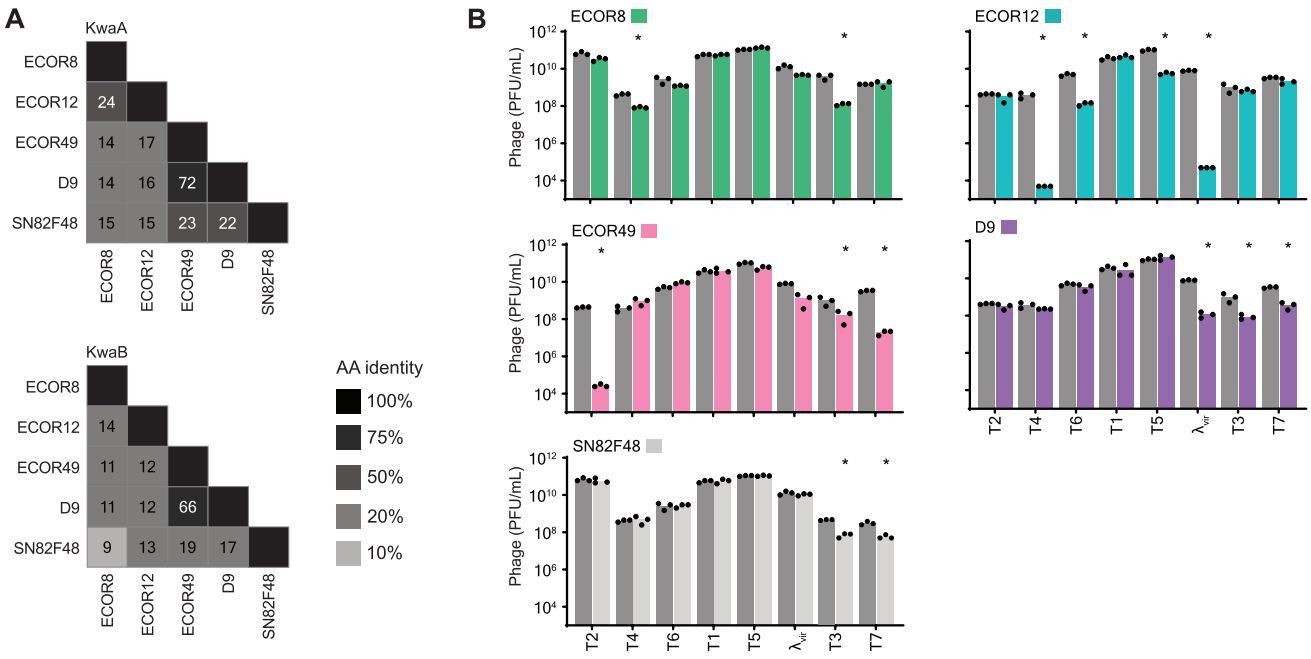

Figure S1. Similarity and anti-phage activity of Kiwa homologues, related to Figure 1

(A) Relative amino acid identity of KwaA and KwaB from experimentally validated systems in this study.

(B) Phage titers from plaque assays testing the Kiwa systems shown in Figure 1D. Bars represent mean (n = 3) with individual points. Open points indicate undetectable individual plaques (value of 1 assigned).

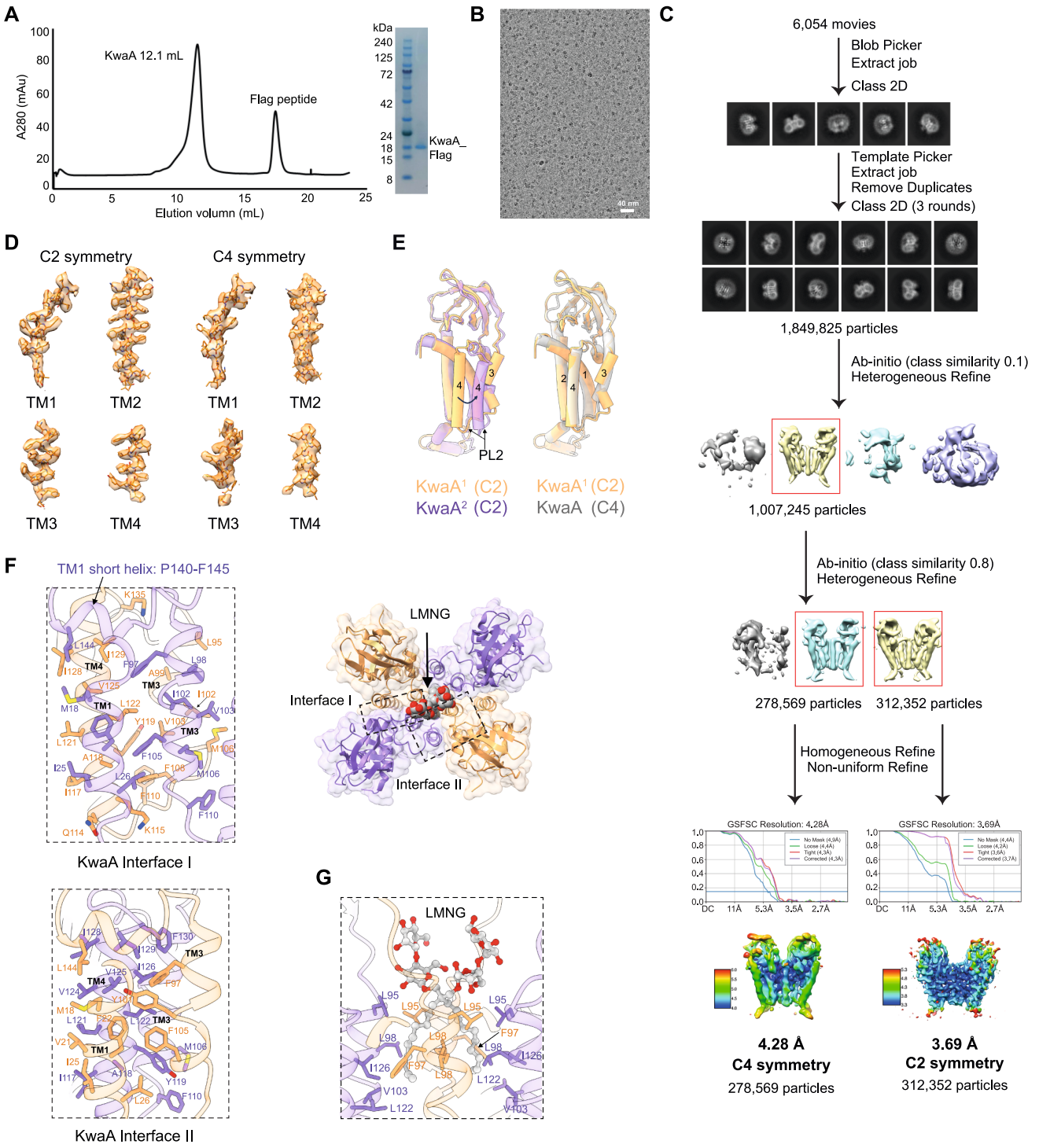

Figure S2. Structure analysis of KwaA, related to Figure 2

(A) Size exclusion chromatography and SDS-PAGE of KwaA tetramer using a Superdex 200 Increase 10/300 GL column.

(B) Representative cryo-EM micrograph of KwaA tetramer.

(C) Cryo-EM KwaA tetramer image processing workflow.

(D) Local density maps of TM1–4 in KwaA tetramers with C2- and C4-symmetry.

(E) Structural alignment of KwaA protomers. Left: comparison within C2-tetramer; right: between C2- and C4-tetramers.

(F) KwaA forms two distinct interfaces in the C2 symmetry. Top right: LMNG interface indicated by an arrow. Top left: interface I, with key hydrophobic residues in TM1 (M18, F22, I25, and L26), and TM3 (F97, L98, I102, V103, F105, M106, and F110) from one protomer and TM3 (L95, A99, I102, V103, M106, and F108) and

(legend continued on next page)

TM4 (I117, A118, L121, L122, V125, I128, and I129) in the adjacent protomer. π-π stacking involves F22, F105, F110, F108, F110, and Y119. TM1 is skewed and interacts via a short helix (P140-F145) with TM4 (L144). Polar contacts are minimal, involving Q114, K115, and K135. Bottom: interface II, with similar hydrophobic and π-π contacts.

(G) LMNG molecule inserted into the C2 KwaA tetramer.

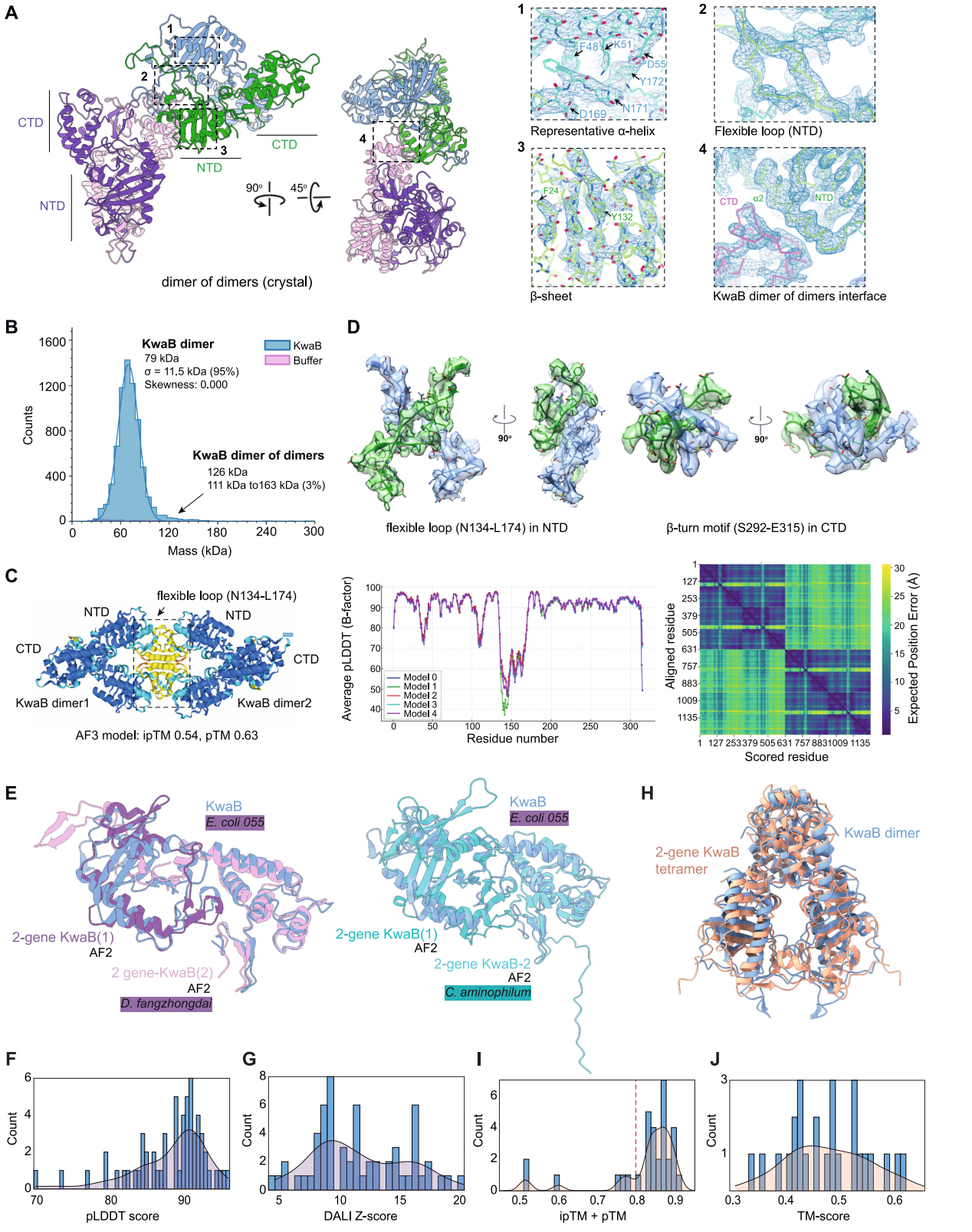

(legend on next page)

Figure S3. Interactions and structural conservation of KwaB multimers, related to Figure 2

(A) Crystal structure of the KwaB dimer-of-dimers from *E. coli* O55, with NTD and CTD labeled and monomers colored differently. Insets show electron density maps in COOT for (1) a representative α-helix, (2) NTD flexible loop, (3) β-sheet region, and (4) dimer-of-dimers interface. Electron density is shown as a blue mesh, and the model as a ribbon or stick.

(B) Mass photometry of KwaB in solution shows a major dimeric species (79 kDa, σ = 11.5 kDa) and a minor oligomeric population (≈3%, ≈126 kDa, range: 111–163 kDa).

(C) AlphaFold3-predicted model of the KwaB dimer-of-dimers. Left: predicted structure with NTD, CTD, and flexible loop (N134-L174) annotated. Middle: pLDDT scores per residue for five models. Right: PAE heatmap.

(D) Cryo-EM density maps of *E. coli* O55 KwaB dimer (Figure 2G) showing the NTD flexible loop (N134-L174) and CTD β-turn motif (S292-E315) from two views.

(E) Superimposition of *E. coli* O55 KwaB with AlphaFold2 models from 2-gene KwaB in *Dickeya fangzhongdai* (Genbank: WP_225622576.1, WP_225622577.1) and *Clostridium aminophilum* (Genbank: WP_074650070.1, WP_074650071.1), colored by phylogenetic cluster as in Figure 1A.

(F) pLDDT score distributions for KwaB monomers from (E), indicating prediction confidence.

(G) DALI *Z* score distribution comparing 2-gene KwaB dimers to *E. coli* O55 KwaB monomer.

(H) Superimposition of *E. coli* O55 KwaB dimer with AlphaFold2-predicted 2-gene KwaB tetramer from *Acinetobacter portensis* (Genbank: WP_163122822.1, WP_163122825.1).

(I) ipTM + pTM scores from AlphaFold2 multimer predictions of 2-gene KwaB tetramers. Only models with a combined score $\geq$ 0.8 were included in (J).

(J) TM-scores comparing tetramer predictions (from I) to the *E. coli* O55 KwaB dimer.

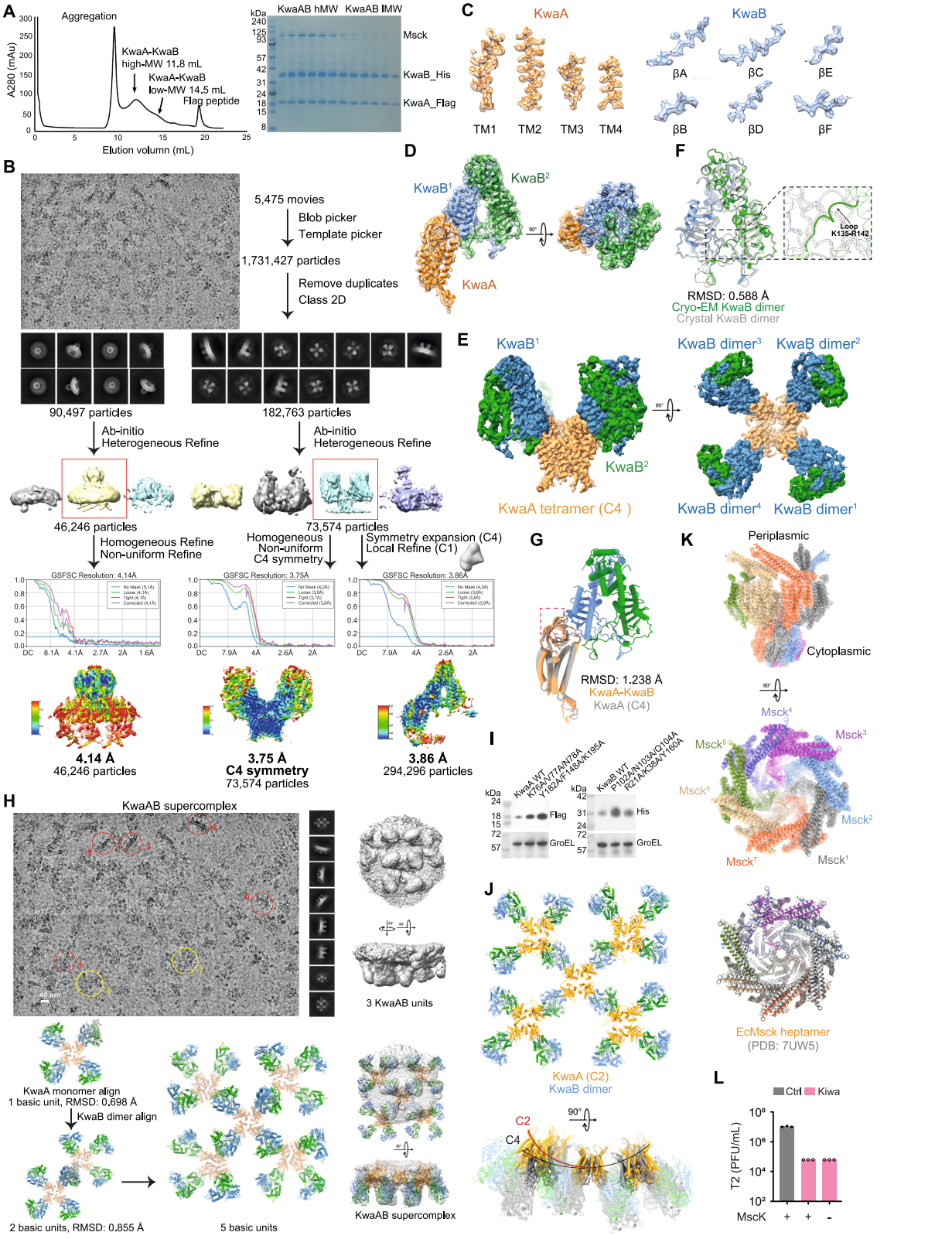

(legend on next page)

Figure S4. Structure analysis of KwaAB, related to Figure 3

(A) SEC (Superose 6 Increase 10/300 GL column) (left) and SDS-PAGE (right) show successful co-expression of KwaAB, revealing high- and low-molecular-weight forms. MscK co-eluted with the high-molecular-weight fraction.

(B) Cryo-EM image processing workflow for high-molecular-weight KwaAB complex. A representative micrograph of the high-molecular-weight complex is shown (top). A 3.86-Å local map was obtained for the KwaA monomer-KwaB dimer unit, and a 4.1-Å map was generated for MscK.

(C) Local density mapping of KwaA TM1–4 (left) and KwaB β-sheets A–F (right).

(D) Map fitting of the KwaA monomer and KwaB dimer.

(E) Two views of the cryo-EM density map of the high-molecular-weight KwaAB complex.

(F) KwaB dimer obtained from cryo-EM (color) and crystallization (silver) shows an RMSD of 0.588 Å.

(G) Alignment of KwaAB dimer and KwaA protomer (C4 symmetry) yields an RMSD of 1.238 Å.

(H) Organization of the KwaAB supercomplex. Top left: representative micrograph and 2D image. Fence-like side views are in red, and top views are in yellow. Top right: cryo-EM density of the supercomplex with three repeating KwaAB units. Bottom: model of the supercomplex built from basic units (KwaA tetramer + four KwaB dimers). RMSD values for intra- and inter-unit alignments are 0.698 and 0.855 Å, respectively. Expansion to five units illustrates higher-order assembly. Bottom right: model fitted into the cryo-EM map.

(I) Western blots showing expression of FLAG-KwaA and His-KwaB variants in *E. coli*. Left: FLAG-KwaA wild-type and loop interface mutants (K76A/V77A/N78A and Y182A/F148A/K195A). Right: His-KwaB wild-type and interface mutants (P102A/N103A/Q104A and R21A/K38A/Y160A). GroEL is loading control.

(J) Modeling shows C4 symmetry induces less membrane curvature than C2 symmetry.

(K) Fitting of *E. coli* MscK heptamer into map reveals a closed-state conformation, matching PDB: 7UW5 (periplasmic gating ring).

(L) Kiwa phage defense activity in *E. coli* BW25113 wild-type and ΔmscK strains. PFU/mL shown as mean ($n = 3$). $^{*}p < 0.05$ (two-way ANOVA).

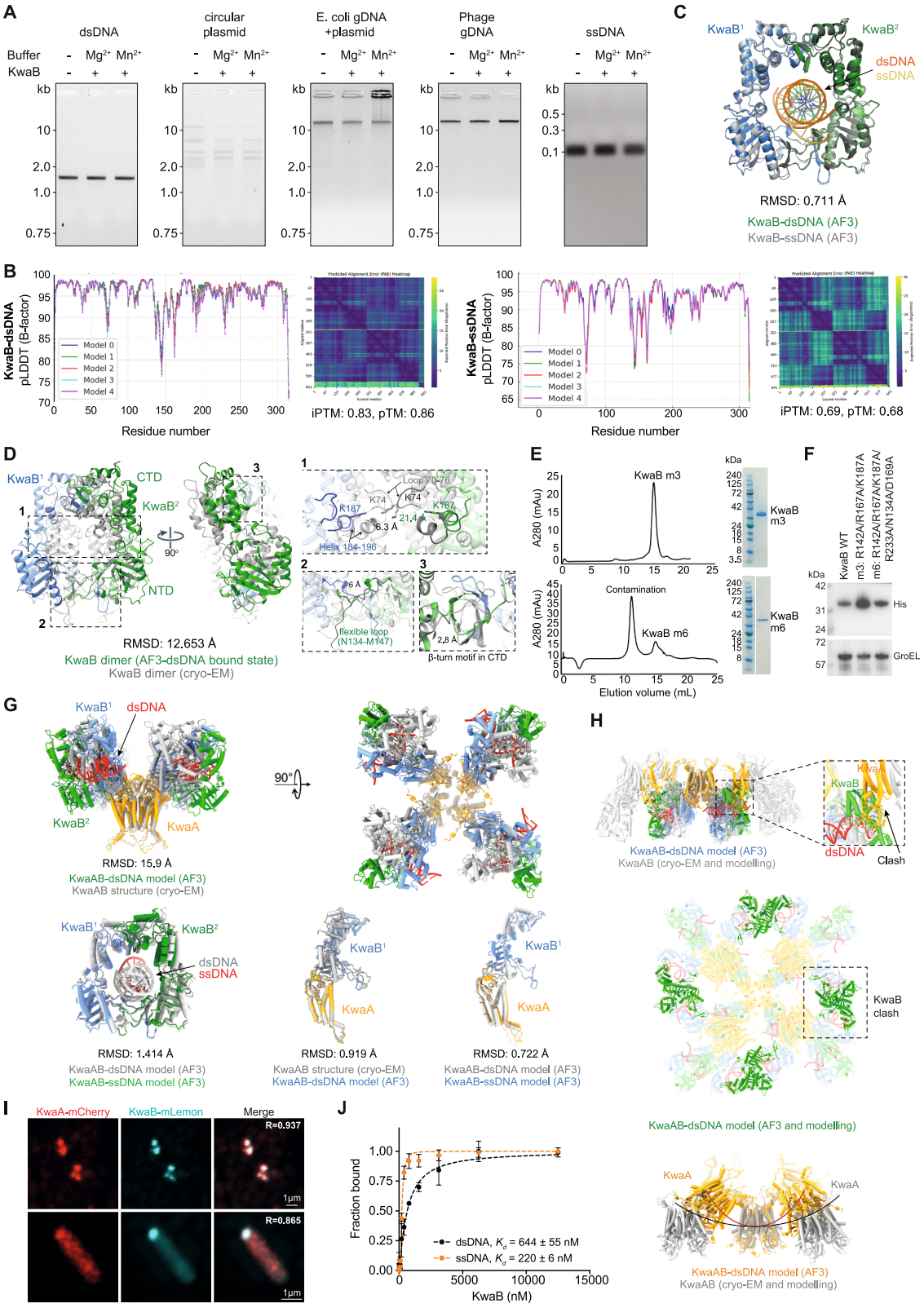

(legend on next page)

Figure S5. KwaB does not degrade DNA, but phage DNA binding blocks replication, related to Figure 5

(A) DNA cleavage assays of KwaB with or without Mg^{2+} and Mn^{2+}. Reactions used 1.14 μM KwaB dimer and either 50 ng dsDNA or 600 ng ssDNA and were subsequently treated with proteinase K and EDTA.

(B) pLDDT and PAE plots for AlphaFold3-predicted KwaB-dsDNA (left) and KwaB-ssDNA (right) models.

(C) Superposition of KwaB-dsDNA (color) and KwaB-ssDNA (silver) models reveals minimal differences.

(D) Conformational changes upon DNA binding: (1) the central pore (loop 70–76 and helix 184–196) rotates ∼43° and shifts 5.5 Å toward the NTD, expanding from 6.3 to 23 Å. (2) Flexible ring (N134–M147) shifts 6 Å inward, enabling interactions. (3) β-motif in CTD moves ∼2.8 Å away from the pore. Overall, CTD rotates 20° counterclockwise and shifts 3.5 Å, while NTD rotates ∼44° clockwise and shifts 10 Å.

(E) SEC (Superdex 200 Increase 10/300 GL column) and SDS-PAGE confirm expression of DNA-binding mutants (m3 and m6).

(F) Western blot detecting His-tagged wild-type and mutant KwaB (m3 and m6) in *E. coli*. GroEL was used as a loading control.

(G) Top: AF3-predicted KwaAB-dsDNA model (4 KwaA, 8 KwaB, and 4 16-mer dsDNA; ipTM 0.46 and pTM 0.49). Bottom left: KwaB-DNA alignment between AF3 KwaAB-dsDNA (silver) and -ssDNA (color). Bottom right: alignment of KwaA-KwaB interfaces from cryo-EM and AF3 models.

(H) Top: superposition of KwaA tetramer (high-order model) and AF3-predicted KwaAB-dsDNA reveals steric clash. Middle: KwaB-KwaB overlap highlights structural conflict. Bottom: such clashes likely distort KwaA conformation, increasing membrane curvature.

(I) Additional examples of KwaA-KwaB co-localization in T2-infected cells (mCherry-KwaA in red and mLemon-KwaB in blue).

(J) Fluorescence anisotropy assays of KwaB (monomeric, nM) to 20-bp ssDNA (red) and dsDNA (black). Data show mean ± SD (n = 3) and the dissociation constants (K_d) for each substrate.

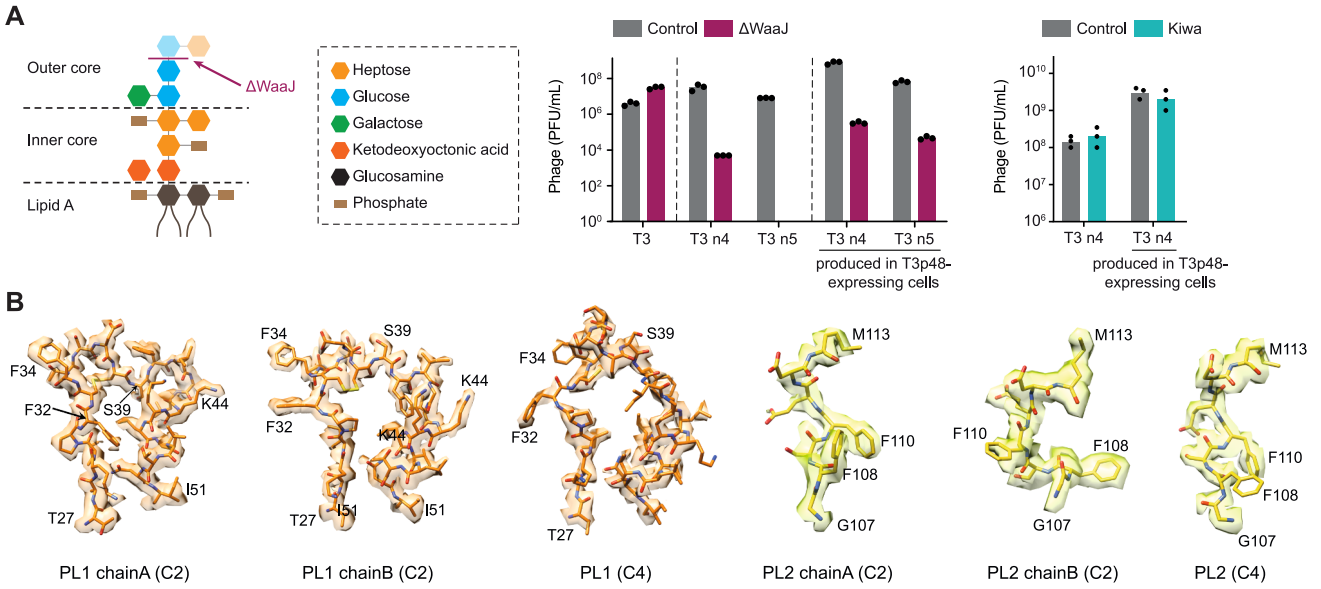

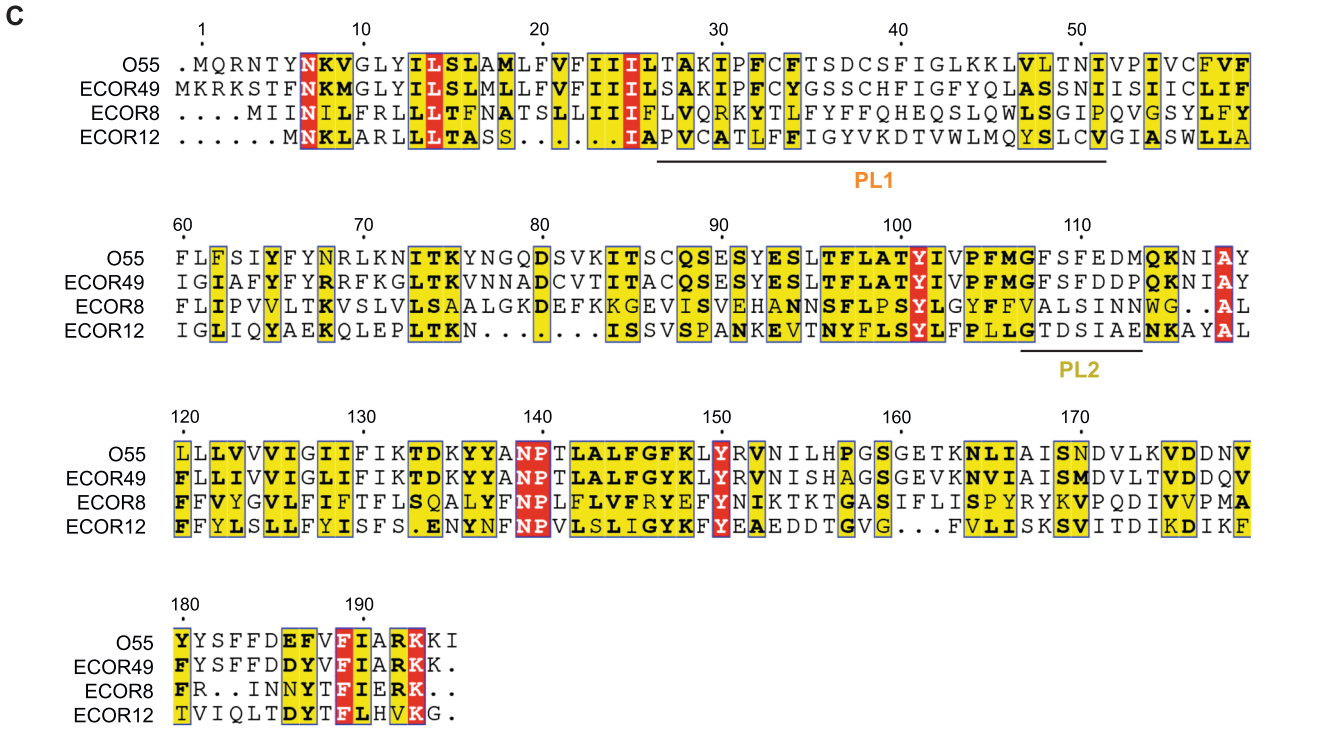

Figure S6. Analysis of Kiwa sensing features, related to Figure 6

(A) Left: schematic of *E. coli* LPS highlighting the ΔwaaJ mutation in the outer core. Middle: plating efficiency of T3 escapers n4 and n5 on ΔwaaJ and control cells. Complementation of T3 n5, but not n4, with wild-type T3p48 in *trans* restores infectivity in ΔwaaJ cells, confirming tail fiber incorporation. Right: phage titers of T3 n4 and its T3p48-complemented version in control and Kiwa cells. Bars show mean ± SD (n = 3).

(B) Electron density fitting of periplasmic loops PL1 (left) and PL2 (right) in KwaA chains A and B (C2-symmetry) and in KwaA with C4-symmetry. PL1 shows high conformational variability. Ribbon and density surfaces are depicted in orange (PL1) and green (PL2).

(C) Sequence alignment of KwaA from O55:H7, ECOR49, ECOR8, and ECOR12, showing poor conservation in PL1 and PL2. Conserved and semi-conserved residues are boxed in red and yellow, respectively.

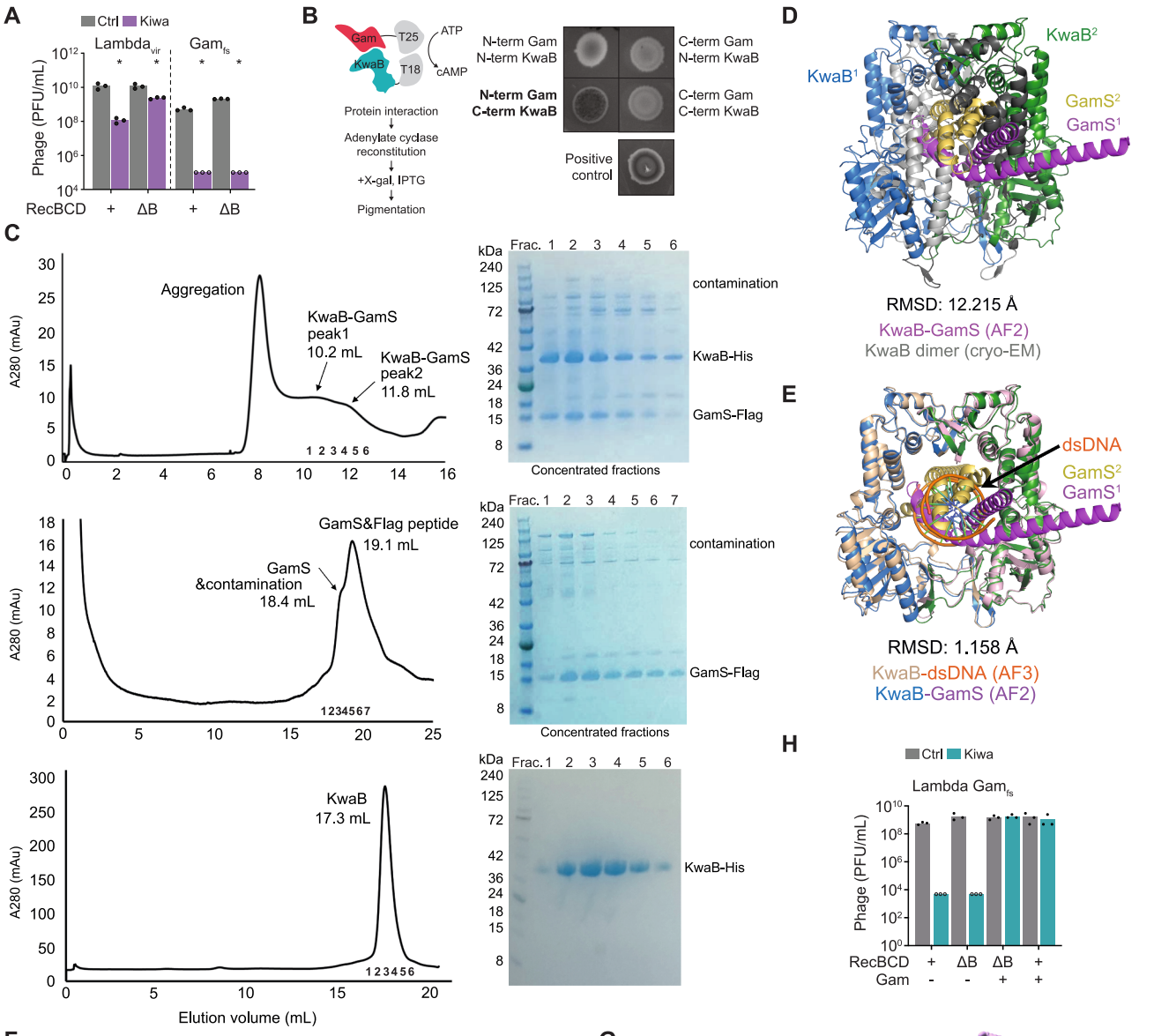

Figure S7. Inhibition of KwaB by Lambda Gam protein, related to Figure 7

(A) Kiwa defense against Lambda$_{vir}$ or a Gam frameshift mutant (Gam$_{fs}$) in RecBCD (+) or ΔRecB (ΔB) cells. Phage titers are shown for control and Kiwa-expressing strains. *$p < 0.05$ (two-way ANOVA). Bars shown mean ($n = 3$) with individual points. Open points indicate undetectable plaques (value of 1 assigned).

(B) Bacterial two-hybrid assay of KwaB and Gam interactions. GCN4 leucine zipper was used as a positive control.

(C) SEC (Superose 6 Increase 10/300 GL column, left) and SDS-PAGE (right) analysis of pull-down assay with Gam-FLAG, KwaB-His, or both proteins.

(D) Structural overlay of cryo-EM KwaB dimer (silver) with AF2-predicted KwaB-GamS complex (color).

(E) Overlay of AF3 KwaB-dsDNA and AF2 KwaB-GamS models.

(legend continued on next page)

(F) pLDDT (left) and PAE (right) plots for AF2 KwaB-GamS models.
(G) Structural exclusivity between RecBCD-Gam (PDB: 5MBV) and AF3-predicted KwaB-Gam.
(H) Kiwa defense against Lambda_Gam_{fs} in $RecBCD^+$ and ΔRecB backgrounds, with or without plasmid-expressed Gam. Bars show mean PFU/mL ($n = 3$) with individual points. *$p < 0.05$ (two-way ANOVA).